



University of
Stavanger

Faculty of Science and Technology

MASTER'S THESIS

Study program/Specialization: Petroleum Geosciences Engineering	Spring, 2013 Open
Writer: Dora Luz Marín Restrepo	
Faculty supervisor: Nestor Cardozo	
External supervisor(s): Camilo Montes, Universidad de Los Andes (Bogota-Colombia)	
Title of thesis: Structural analysis of the Tabaco anticline, Cerrejón mine, Northern Colombia (South America)	
Credits (ECTS): 30	
Keywords: Strain, curvature, restoration, strike slip fault, throw, 3D model	Pages: 71 Stavanger, June 13, 2013

Copyright
by
Dora Luz Marín Restrepo
2013

**Structural analysis of the Tabaco anticline, Cerrejón mine, Northern
Colombia (South America)**

by

Dora Luz Marín Restrepo

Master Thesis

Presented to the Faculty of Science and Technology

The University of Stavanger

The University of Stavanger

06-2013

Acknowledgements

I would like to thank my supervisors Nestor Cardozo and Camilo Montes for their help with preparation and processing of the data, as well as for their valuable comments, edits and constructive discussions. Thanks to Dave Quinn at Badleys for his fast and effective answers about TrapTester, which were crucial to accomplish my goals. I would also like to thank Chris Townsend for help in the construction of the 3D model, and Lisa Bingham for help with ArcGis. Finally, thanks to Andreas Habel for IT support. The computers programs TrapTester (Badleys), 3DMove (Midland Valley), Petrel (Schlumberger), Matlab (Mathworks), and OSXStereonet (Cardozo and Allmendinger, 2013) were used in this thesis.

Abstract

Structural analysis of the Tabaco anticline, Cerrejón mine, Northern Colombia (South America)

Dora Luz Marín Restrepo

University of Stavanger, 2013

Supervisor: Nestor Cardozo Ph.D.

External Supervisor: Camilo Montes Ph.D.

The Tabaco anticline is located in the Cesar-Ranchería basin of northern Colombia, South America, close to the transpressional collision between the Caribbean and South American plates. The anticline is bounded by the Cerrejón thrust to the east, the right lateral strike slip Oca fault to the north, and the left lateral strike slip Ranchería fault to the south. The anticline is asymmetric and verges to the SE, with a NW limb dipping in average 26°W , a SE limb dipping 41°E , and a fold axis $217^{\circ}/7^{\circ}$ (trend and plunge). The fold's vergence is opposite to that of the Cerrejón thrust. In this thesis, I make a 3D structural model of the Tabaco anticline using a high resolution dataset from the Cerrejón open coal mine in an area of about 10 km^2 . This 3D model contains 17 coal seams and 67 faults. The thesis is divided in three main parts: Construction of a 3D structural model, fault displacement analysis, and restoration of the anticline. Four different patterns in the contours of fault throw were observed: 1) Low throw in the middle of the fault and high throw in the areas around, 2) Highest throw at one corner of the fault and not in the center, 3) Highest throw in the middle of the fault, and 4) In conjugated faults, highest value of throw at the intersection of the two fault planes. Most of the faults show pattern 3. Patterns 1 and 2 are mostly due to lack of sampling of the entire fault surfaces. Faults show a consistent pattern of slip in the area. 3D restoration of the anticline using a flexural slip technique suggests a total

shortening of 18%. Fault-related strain (from the analysis of fault displacement) and fold-related strain (from the restoration of the coal seams) are related, with the highest values of fold-related strain associated with a fault in the core of the anticline, and the faults located in the SW anticlinal limb. Fold-related strains are also high in the SE, steeply dipping anticlinal limb. The results of this study show that the anticline was affected by uplift of the Santa Marta massif, Perijá range deformation, and strike-slip movement of the Oca , Samán and Ranchería faults.

Table of Contents

List of Tables.....	viii
List of Figures.....	ix
1 Introduction.....	11
2 Geological setting.....	15
2.1 Regional tectonic setting.....	15
2.2 Cenozoic stratigraphy of the Cesar-Ranchería Basin.....	18
2.3 The Tabaco Anticline and the Cerrejón mine data.....	19
3 Methods.....	26
3.1 Construction of 3D structural model.....	26
3.1.1 Coal seams construction.....	26
3.1.2 Fault network construction.....	28
3.2 Fault displacement analysis.....	29
3.3 Restoration of the anticline.....	30
3.4 Curvature.....	32
4. Results.....	33
4.1 3D structure of the Tabaco anticline.....	33
4.1.1 Fault geometry.....	33
4.1.2 Curvature.....	39
4.2 Fault displacement analysis.....	43
4.2.1 Fault displacement patterns.....	43
4.2.2 Fault array summation and strain.....	45
4.3 Restoration.....	54
4.3.1 Strain maps.....	57
5. Discussion.....	59
5.1 Summary of the main events affecting the Tabaco anticline in a regional context.....	63
References.....	66

List of Tables

Table 1. Summary of main faults in the area.....	17
---	----

List of Figures

Figure 1. Location of the study area in Northern Colombia (South America).....	12
Figure 2. Geologic map of the northern Cesar-Ranchería Basin in the area of the Tabaco anticline.....	13
Figure 3. Schematic illustration of an isolated fault.....	14
Figure 4. Generalized Cenozoic stratigraphy of the northern Cesar-Ranchería Basin.....	16
Figure 5. Systematic dissection of the Tabaco Anticline in ten horizontal mining levels.....	22
Figure 6. Map showing the location of measured bedding data (red lines) in the Tabaco anticline.....	23
Figure 7. Lower hemisphere stereographic projection of poles to bedding in the Tabaco anticline.....	24
Figure 8. Lower hemisphere stereographic projection of poles to bedding from reconstructed coal seams surfaces in the Tabaco anticline.....	24
Figure 9. Down-plunge projection of the Tabaco anticline.....	25
Figure 10. Steps in the construction of the coal seam surfaces.....	27
Figure 11. Steps in the construction of a fault plane.....	29
Figure 12. a) Map showing the location of the cross sections A-A', B-B' and C-C' b) Three cross section of the Tabaco anticline after the reconstruction of upper coal seams with parallel folding.....	32
Figure 13. Geologic curvature classification.....	33
Figure 14. Faults in the 3D model and their occurrence in each of the coal seams.....	39
Figure 15. Distribution of maximum curvature (k_{max}), minimum curvature (k_{min}), and geologic curvature with $kt = 0$	42
Figure 16. Fault throw patterns observed in the 3D model.....	44
Figure 17. Distribution of fault patterns in coal seam 130.....	45
Figure 18. Left side: Maps displaying the faults affecting each coal seam, contoured by their throw attribute. Right side: Plots of individual and cumulative fault throw, and cumulative	

fault related strain vs. distance. The initial and the last position of the sampling line are indicated in the map view. **e-o** contain two groups of plots, one corresponding to NW-SE striking faults, and another to NE-SW striking faults.....54

Figure 19. Restoration of the Tabaco anticline using the flexural-slip technique.....56

Figure 20. Maps of maximum principal elongation (e1).....58

Figure 21. Stearn and Friedman (1972) model showing the fractures set associated with folding.....60

Figure 22. Individual and aggregate fault throw, and fault-related strain vs. distance for coal seam 123 after the re-interpretation of fault 4.....61

Figure 23. Summary of the main events affecting the Tabaco anticline.....66

1. Introduction

3D structural models allow the integration of scattered 2D and 3D data (e.g. field mapping, 2D and 3D seismic, wells) into a common framework, where the data must complement each other and give rise to an internally consistent model. There are beautiful examples of 3D models, particularly in areas where the data have very high resolution, large coverage, and are measured on 2D slices of various orientations (e.g. Yorkshire coal mines data in the UK). Integration of these data in 3D has given us tremendous insight into the geometry, displacement fields and growth of faults, particularly in extensional settings (e.g. Rippon 1985; Walsh and Watterson, 1987, 1988; Huggins et al, 1995). Restoration of 3D structural models is a great tool to better understand the spatial and temporal evolution of geological structures, and in the subsurface where often only seismic and sparse well data are available, it is the most relevant tool to predict subseismic features such as fractures. 3D structural models are thus key to represent and characterize reservoirs. They are the basic framework of hydrocarbon flow models. Inconsistencies in 3D structural models (e.g. incorrect positioning of the fault network and layer juxtapositions) have higher impact on fluid flow models than the exact calibration of fluid flow model parameters (Fisher and Jolley, 2007).

In this thesis, I make a 3D structural model of the Tabaco anticline, using a high resolution dataset from the Cerrejón open coal mine in La Guajira department, northern Colombia, South America (Figure 1). The dataset consists of differential GPS measurements of coals seams and fault traces on 10 horizontal slices (i.e. mining levels) in an area of about 10 km². These coal seams delineate the geometry of the anticline in 3D. Additionally, this dataset offers an unique opportunity to understand faulting and folding in a transpressional setting, in an area bounded by regional strike-slip faults to the north and south, and a thrust to the east. This study is a continuation of previous research by Montes et al. (in prep.) who acquired and processed the GPS data, measured kinematic indicators in the area, and constructed a pseudo-3D model of the anticline.

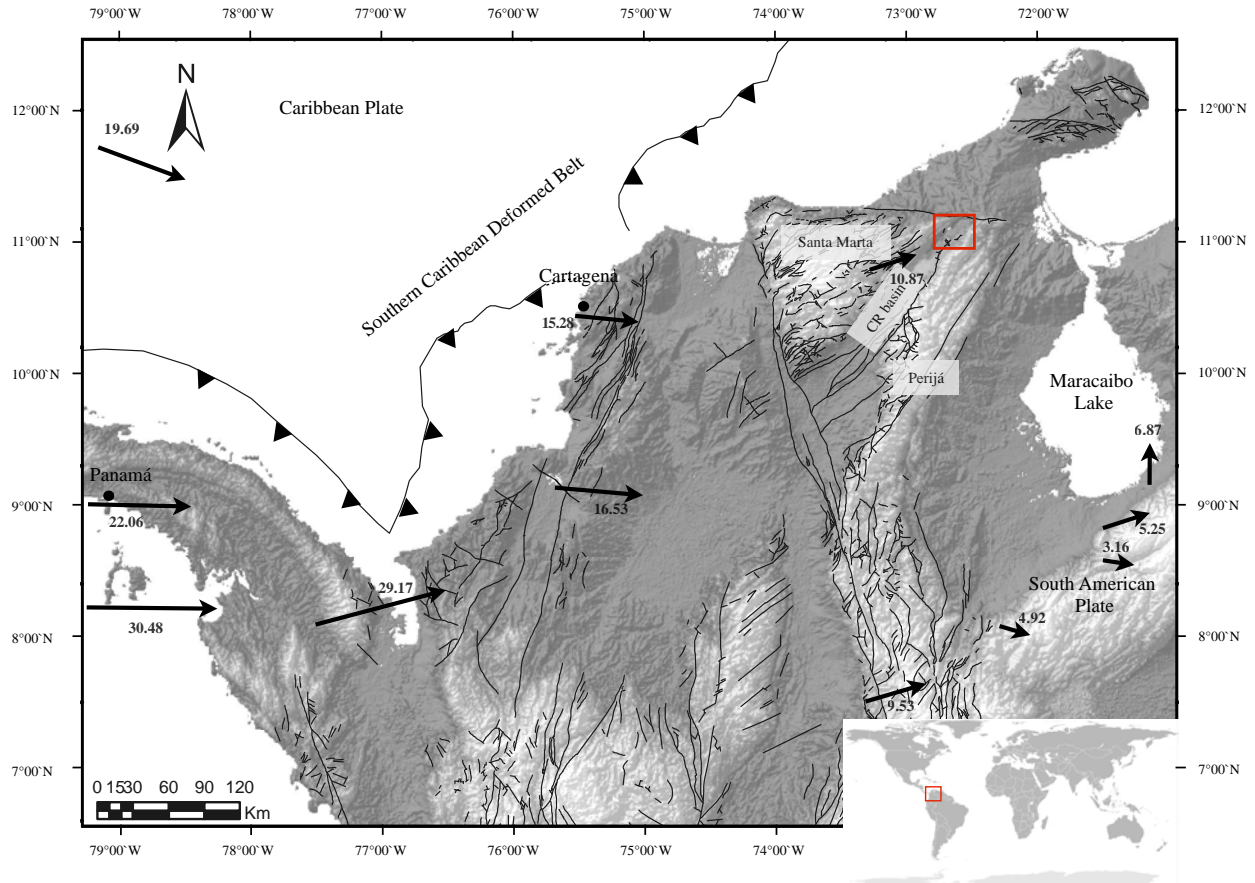


Figure 1. Location of the study area in Northern Colombia (South America). The red rectangle is the study area (Figure 2). Black lines are faults. CR = Cesar-Ranchería Basin. Black arrows are GPS velocity vectors relative to stable South America (1991, 1994, 1996, and 1998 CASA campaigns; Trenkamp et al., 2002). Numbers are velocity vectors in mm/yr.

The Tabaco anticline is located in the Cesar-Ranchería Basin of Northern Colombia, South America, close to the transpressional collision between the Caribbean and South American plates (Figure 1). The anticline is an asymmetric fold plunging to the southwest (Ruiz, 2006; Palencia, 2007). The asymmetry of the fold is defined by steeply dipping strata (average of 41°E) on its southeastern flank, and shallowly dipping strata (average of 26°W) on its northwestern flank (Montes et al., in prep.). The Tabaco anticline is bounded to the southeast by the northwest-verging, Cerrejón thrust (which is also the boundary between the Cesar-Ranchería Basin and the Perijá range), to the north by the right-lateral Oca fault, to the south by the left-lateral Ranchería fault, and to the west by the 5700 m high Santa Marta massif (Figure 2). The trend of the anticline ($\text{N}20^{\circ}\text{E}$) is oblique to the Oca and Ranchería strike-slip faults, and its vergence is

opposite to that of the Cerrejón thrust (Montes et al., 2010). The Tabaco anticline is important for the geology of the area because it records the deformation of the strike-slip and thrust faults, and the uplift of the Santa Marta massif and Perijá range.

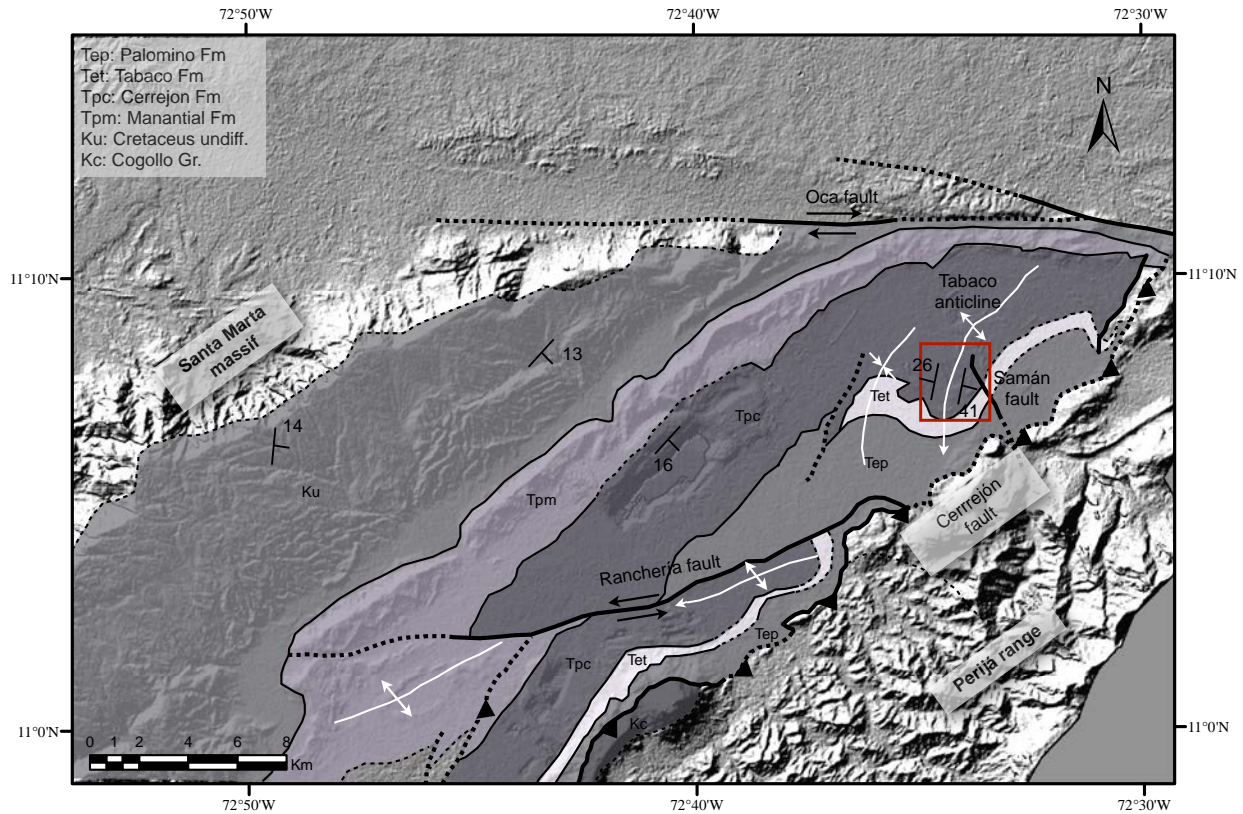


Figure 2. Geologic map of the northern Cesar-Ranchería Basin in the area of the Tabaco anticline. Modified from Montes et al. (2010). The red rectangle shows the area of the Cerrejón open coal mine where the GPS data were collected.

This thesis is subdivided in three main topics: Construction of a 3D structural model, fault displacement analysis, and restoration of the anticline. The 3D model of the anticline was constructed using the traces of coal seams and faults on horizontal mining levels, giving a total of 17 coal seams and 67 faults. The faults were divided into four structural domains as suggested by Palencia (2007). The 3D model was used to calculate the displacement field on faults. An important concept is that the faults should show a reasonable variation in displacement, with zero displacement at the fault tipline and maximum displacement at the center of the fault surface (Kim and Sanderson, 2005; Figure 3).

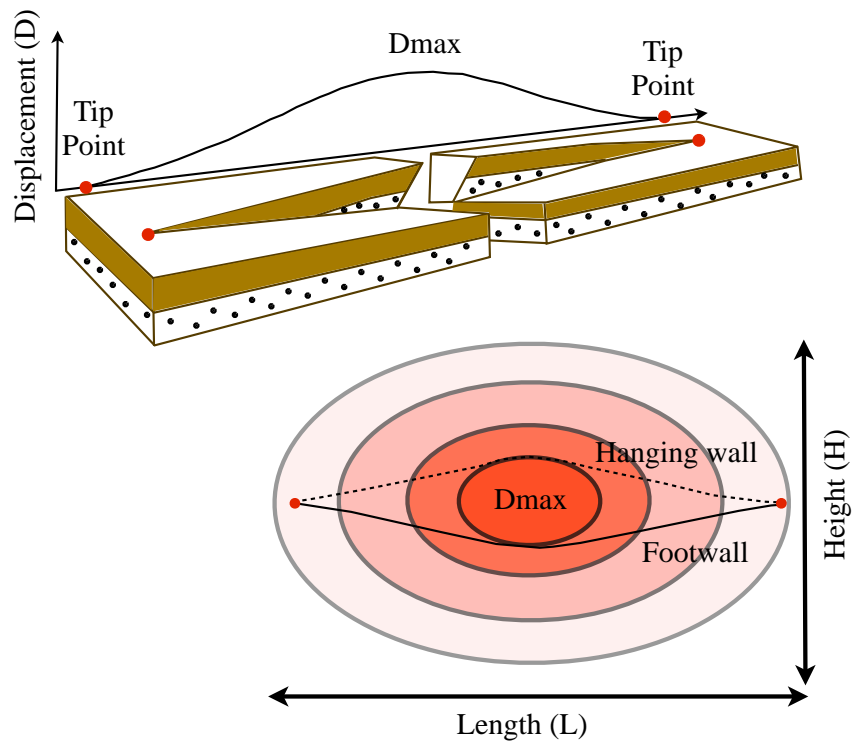


Figure 3. Schematic illustration of an ideal, isolated fault. Displacement is maximum at the center of the fault and decreases outwards to be zero at the fault tipline (modified from Fossen, 2012).

Using TrapTester (Badleys), the throw was calculated on each fault. Four different patterns in the contours of fault throw were found: 1) Low throw in the middle of the fault and high throw in the areas around, 2) Highest throw at one corner of the fault and not in the center, 3) the most common pattern, highest throw in the middle of the fault, and 4) In conjugated faults, highest throw at the intersection of the two fault planes.

Pattern 1 can be explained by the fault linkage model (Peacock and Sanderson, 1991; Cartwright et al., 1995), in which the faults grow as isolated faults at early stages and then link to produce larger faults. In this case, the area of low throw is indicating the zone of fault linkage. A possible explanation for pattern 2 is that the fault is actually larger, but there are not enough data to

resolve the complete fault plane. Pattern 3 is the consistent pattern of fault displacement of Figure 3. In pattern 4, the two conjugate faults add to a larger displacement.

Profiles of fault displacement versus distance were also constructed to visualize the 3D distribution of fault displacement in the anticline, and to make inferences about fault-related strain (i.e. the gradient of fault displacement) in the area. The faults with highest value of throw are fault 59 (an E-W fault located in the core of the anticline), and fault 45 (the Samán fault). The faults that show the highest values of strain are located in the SW limb of the anticline and have a strike NE-SW.

Finally a restoration of the Tabaco anticline was performed using a flexural-slip technique. This technique preserves volume in 3-D, line length in the unfolding direction, and orthogonal bed thickness (Griffiths et al., 2002). The restoration shows that the total shortening of the Tabaco anticline is 18%. The shortening of coal seam 130 is 6%, 115 is 2%, 105 is 7%, and 100 is 3%. The maximum fault-related strain for coal seam 130 is 5%, 115 is 3%, 105 is 10 % and 100 is 2.5%. The results of this study show that the anticline was affected by the uplift of the Santa Marta massif and Perijá range, and the strike slip movements of the Oca, Samán and Ranchería faults.

2 Geological setting

2.1 Regional tectonic setting

The Tabaco anticline is located in the Cesar-Ranchería basin, northern Colombia, South America, close to the transpressional collision between the Caribbean and South American plates (Figure 1). The northern part of the Cesar-Ranchería basin is defined by a southeast-dipping monocline that shows structural continuity with the Santa Marta massif to the west (Figure 2). The monocline is bounded to the north by the right-lateral Oca fault and to the east by the northwest-vergent Cerrejón thrust (Montes et al., 2010) which limits the Perijá range (Kellogg, 1984; Figure 2). Faults and folds in the footwall of the Cerrejón thrust are only affecting Cenozoic

rocks (Figure 4), these structures include the left-lateral Ranchería fault and the Tabaco anticline (Montes et al., 2010). Table 1 shows a summary of the main faults in the area. Sánchez and Mann (2012) describe 3 major periods of shortening for the Cesar-Ranchería Basin that include: an event in the Paleocene- early Eocene, an Oligocene- early Miocene event, and a last period in the Pliocene-Pleistocene.

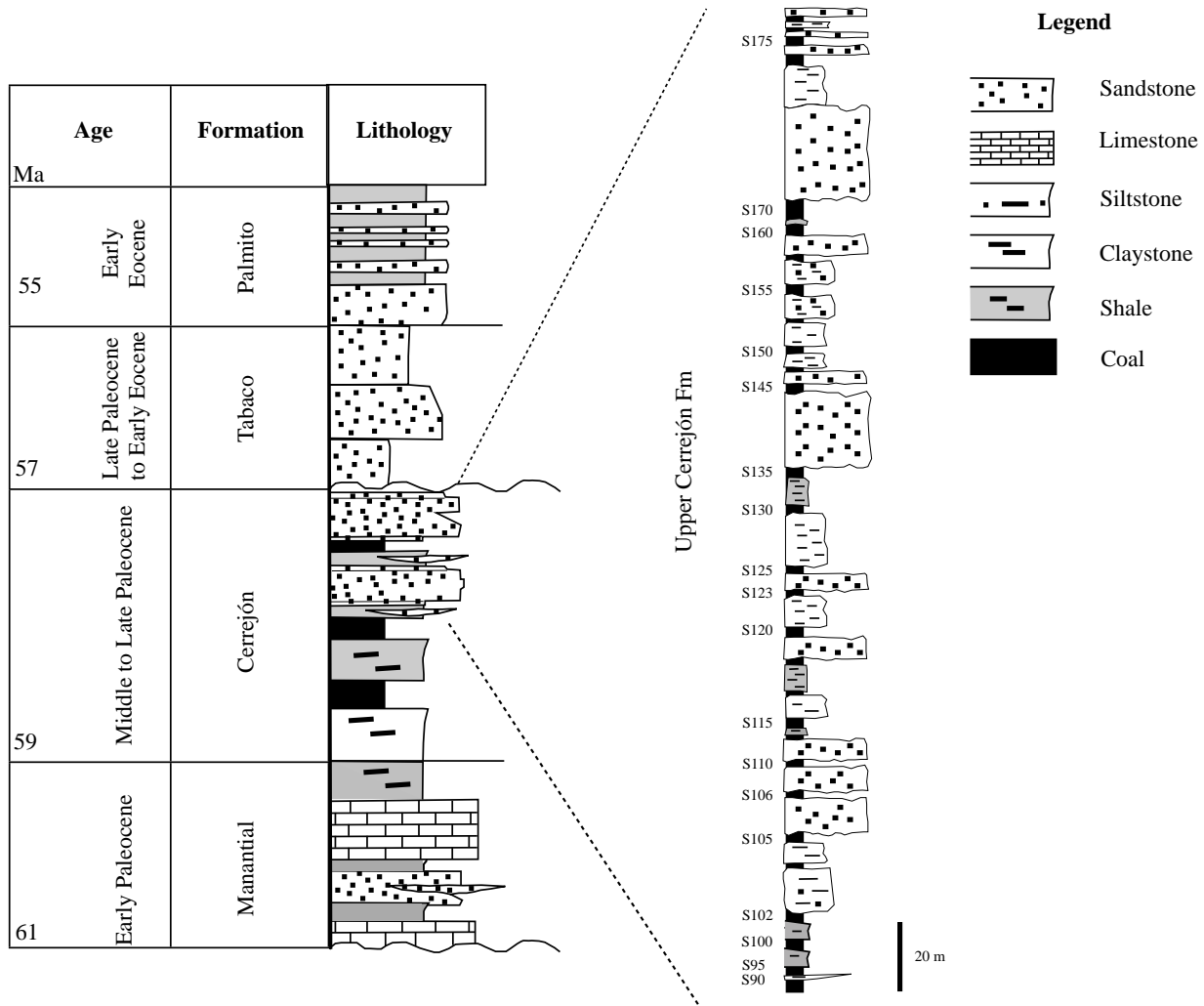


Figure 4. Generalized Cenozoic stratigraphy of the northern Cesar-Ranchería Basin and detail of the Upper Cerrejón Formation where the coal seams (S) analyzed in this study are located. Identification numbers on the coal seams are the same as those of the 3D model (modify from Bayona et al., 2011).

Table 1. Summary of main faults in the area

Name of Fault	Type	Displacement	Age
Oca	Right lateral strike slip	Feo-Codecido (1972): 15 to 20 km Tchanz et al. (1974): 65 km Montes et al. (2010): 75-100 Km Kellogg (1984): 90 km Pindell et al. (1998): 100 km	Middle to Late Miocene (Konn in Shagam, 1984)
Cerrejón	Reverse	Total throw between 16-26 km (Kellogg and Bonini, 1982)	Early Eocene and Late Oligocene (Montes et al., 2010)
Ranchería	Left lateral strike slip	5 km (Sánchez, 2008; Montes et al., 2010)	No information available

The western boundary of the area is the Santa Marta massif (Figure 2), an isolated, triangular basement block with a maximum elevation of 5700 meters above sea level. Cardona et al. (2008) estimated exhumation rates for the Santa Marta massif of 0.7 km/Ma between 65-48 Ma, 0.16 km/Ma until the Late Oligocene, and 0.33 km/Ma in the middle-late Miocene.

The eastern limit of the Cesar-Ranchería basin is the northwest-vergent Cerrejón thrust with an average dip of 9-12° towards the SE in the surface (Montes et al., 2010). This fault is the western boundary of the Perijá range (Figure 2). The Perijá range consists of Mesozoic and Palaeozoic igneous and sedimentary rocks with a maximum elevation of 3650 meters above sea level (Kellogg, 1984). Four deformation phases have been described in the area starting in the Early Eocene (53 Ma) and Middle Eocene (45 Ma), intensifying during the Late Oligocene with thrust sheet emplacement and unroofing of 3–4 km (Kellogg, 1984), and ending between the Late Miocene to recent. Four post-Jurassic, thrust detachment levels have been proposed in the Sierra de Perijá: at the base and top of the Upper Cretaceous shales of the Colón Formation, at the shales of the Guaimaros Member of the Cretaceous Apón Formation, at the shale and sandstone with high mica content of the Lisure Formation; and an intrabasement detachment level (Duerto et al., 2006).

2.2 Cenozoic stratigraphy of the Cesar-Ranchería Basin

A Late Cretaceous to Eocene sedimentary succession is preserved in the area (Figure 4). The Early Paleocene Manantial Formation is composed of glauconitic shales and sandy limestones (Bayona et al., 2011). The upper Manantial Formation include calcareous sandstone and biomicrite beds, followed by a thick succession of dark-coloured mudstone and siltstone beds with plant remains and signs of bioturbation. Towards the top, calcareous and fossiliferous sandstone beds interbedded with laminated mudstone and siltstone beds and local conglomerates occur. Bayona et al. (2011) described a change in thickness of this unit eastward from 600 m at the west of the basin, to 180 m in a well close to the Ranchería fault.

The Cerrejón Formation is a 1 km thick coal-bearing unit that consists of very fine to fine grained argillaceous sandstones, dark colored sandy siltstones and interbedded mudstones, shales and coal seams (Bayona et al., 2011). Jaramillo et al. (2007) established an age of Middle-to-Late Paleocene for this formation. The Cerrejón Formation is a deltaic sequence that were deposited in less than 2 My (Bayona et al., 2007; Jaramillo et al., 2007). Almost all the coal seams that were modeled in this thesis are located in the upper part of the Cerrejón Formation (S 100-175, Figure 4), only coal seams 90 and 95 are located in the lower part of the Formation. Provenance analyses in the Paleocene Manantial and Cerrejón Formations in the northernmost part of the Cesar-Ranchería valley indicate that these Formations were supplied from the Santa Marta massif (Cardona et al., 2010; Bayona et al., 2007), indicating uplift of the massif from the Paleocene.

The Late Paleocene-Early Eocene Tabaco Formation is a 75 m thick unit that includes variedly colored, massive mudstone beds interbedded with cross-bedded conglomeratic sandstone beds (Bayona et al., 2011; Cardona et al., 2010). Montes et al. (2010) interpret the Tabaco Formation as syntectonic strata based on thickness changes and field relations with the Cerrejón Formation. They suggested that mild deformation took place in the Cesar-Ranchería basin during the accumulation of this Formation. Provenance analyses in these syntectonic strata indicate a source of the Santa Marta massif (Cardona et al., 2010), but also point to tectonic activity of the Perijá

range (Bayona et al., 2007). Finally, the Palmito Formation (Early Eocene) is composed of light-colored, massive mudstones (Bayona et al., 2011). Beck (1921) estimated a thickness of 60 m for this Formation.

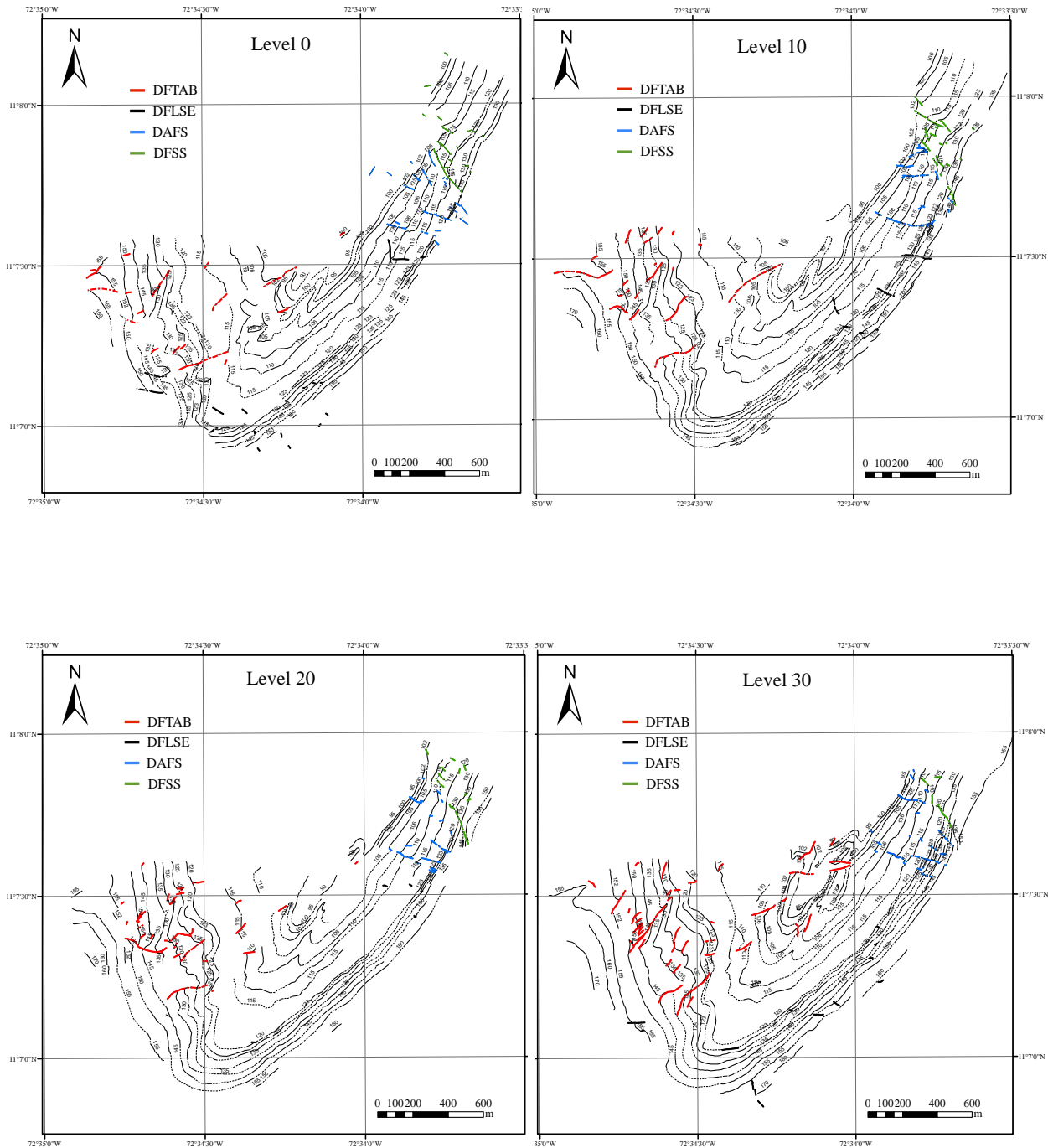
2.3 The Tabaco Anticline and the Cerrejón mine data

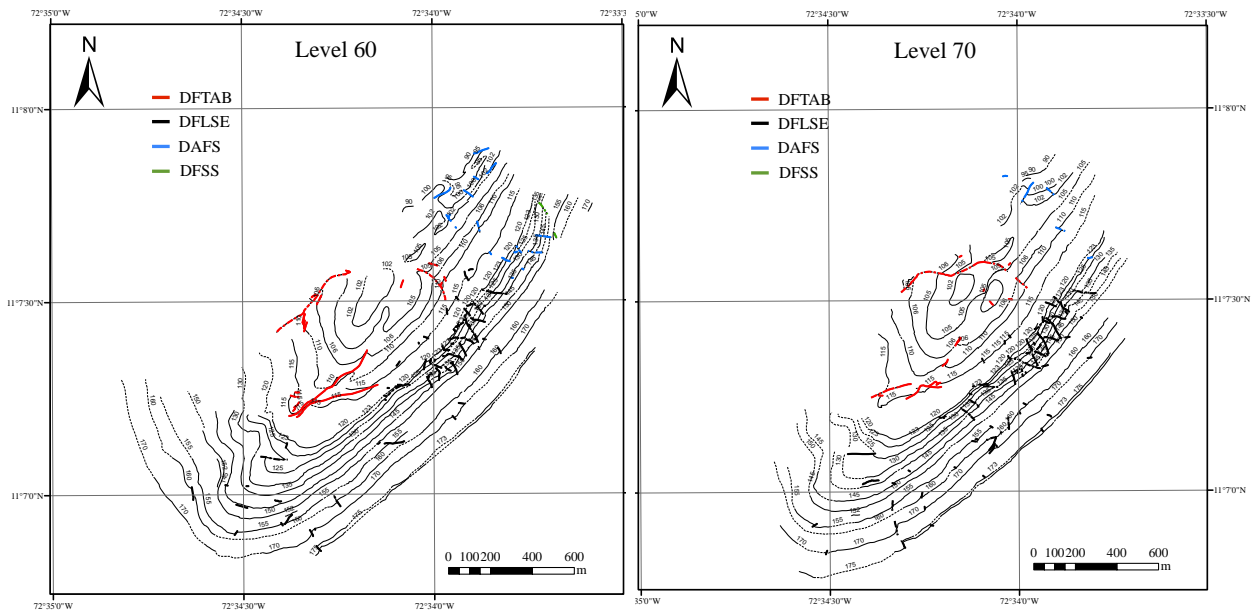
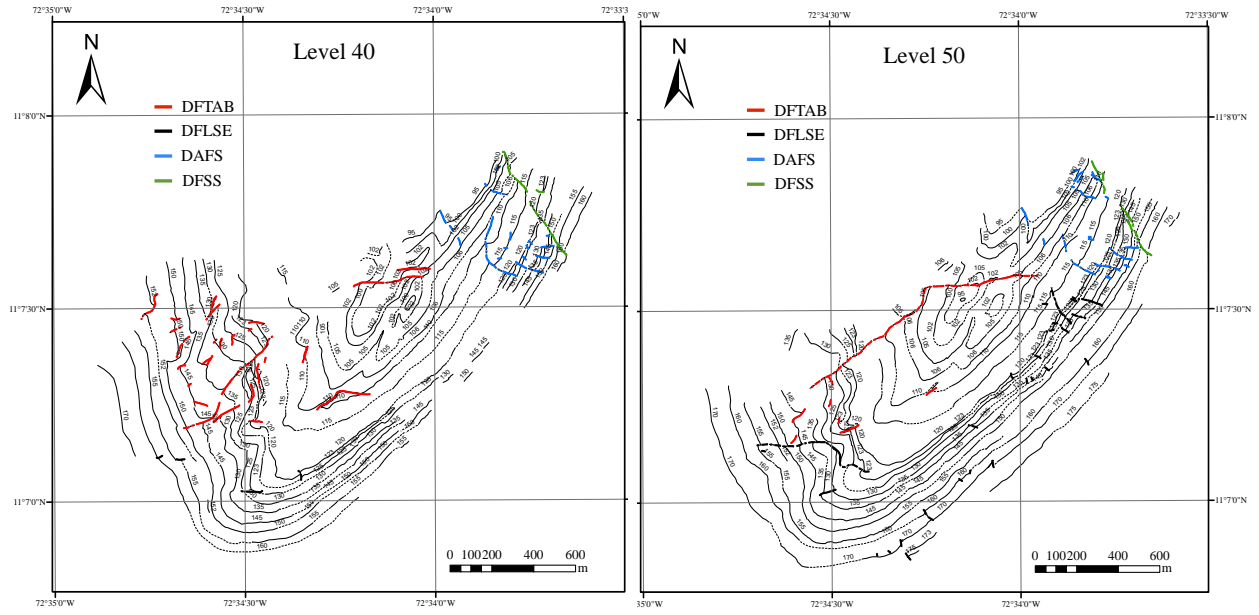
The Tabaco anticline is an asymmetric fold plunging to the southwest (Ruiz, 2006; Palencia, 2007). The asymmetry of the fold is defined by steeply dipping strata (average of 41°E) on its southeastern flank, and shallowly dipping strata (average of 26°W) on its northwestern flank (Montes et al., in prep.). The anticline affects Cenozoic rocks, including the Upper Cerrejón Formation where the coal seams analyzed in this study are (Figure 4).

I use in this thesis a dataset collected in the Cerrejón open coal mine (red square in Figure 2) by several geologists working in the mine. The data are the result of routine in-pit mapping of the intersection of dipping coal seams and horizontal mining levels (Montes et al., in prep.). Each coal seam intersection was followed with differential GPS. Attributes such as the name of the seam, elevation, roof and floor lithologies, dip angle, and apparent thickness along the dip direction were recorded. Structural features such as faults, minor folds, bedding, kinematic indicators (minor folds and slickensides) were also recorded. All this information was stored in a GIS database (Montes et al., in prep.). The coal seams and fault traces in the GIS project were cleaned and interpreted (Montes et al., in prep.). This “clean” database is the initial information for this thesis.

The GIS project contains the traces of 19 coal seams in 10 horizontal mining levels, and more than 1000 fault traces (i.e. fault intersections with the mining levels). The stratigraphic position of the coal seams is shown in Figure 4. The faults are classified by their level of confidence as observed, interpolated or inferred. Figure 5 shows the 10 mining levels. Of the 19 mapped coal seams, 17 were used in the construction of the 3D model. Coal seams 90 and 175 (Figure 4) were not used because there are not enough data to reconstruct them. A limitation of the dataset is that

as the layers become younger, the data coverage becomes less in the core of the anticline. Younger coal seams are only mapped in the limbs of the anticline.





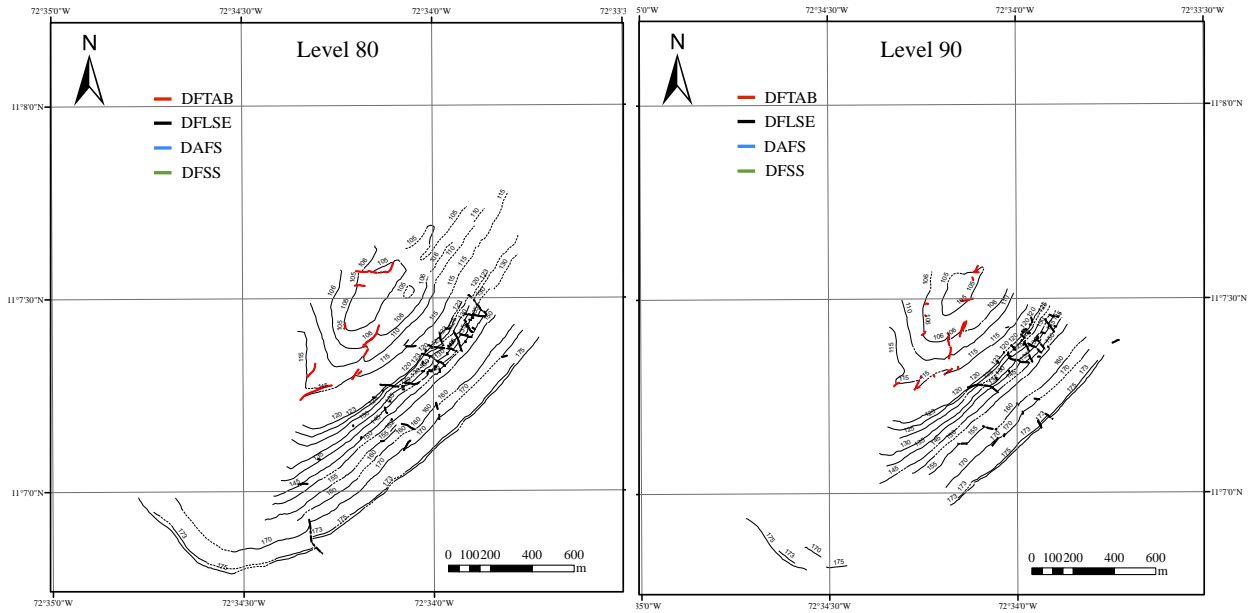


Figure 5. Coal seams (black lines with identification numbers) and fault traces (colored lines) in ten horizontal levels in the Cerrejón mine. Number on level is its elevation a.s.l. in meters. Faults are colored according to the structural domains defined by Palencia (2007). DFTAB : Tabaco fault domain, DFLSE: Southern limb domain, DAFS: Samán antithetic fault domain, DFSS: Samán fault domain.

488 bedding measurements were taken by geologists in the Cerrejón mine (Montes et al., in prep.). The bedding information is located in all mining levels in both, the core of the anticline to the north of the modeled coal seams, and in the limbs of the anticline where there are GPS data (Figure 6). A cylindrical best fit to the data suggests that the anticline is roughly cylindrical, with a fold axis (trend and plunge) 217/7 (Figure 7). Strike and dip data from the reconstructed coal seam 3D surfaces (best-fit plane routine of Fernandez, 2005 in 3DMove) suggest also a roughly cylindrical fold with a fold axis 204/5 (Figure 8).

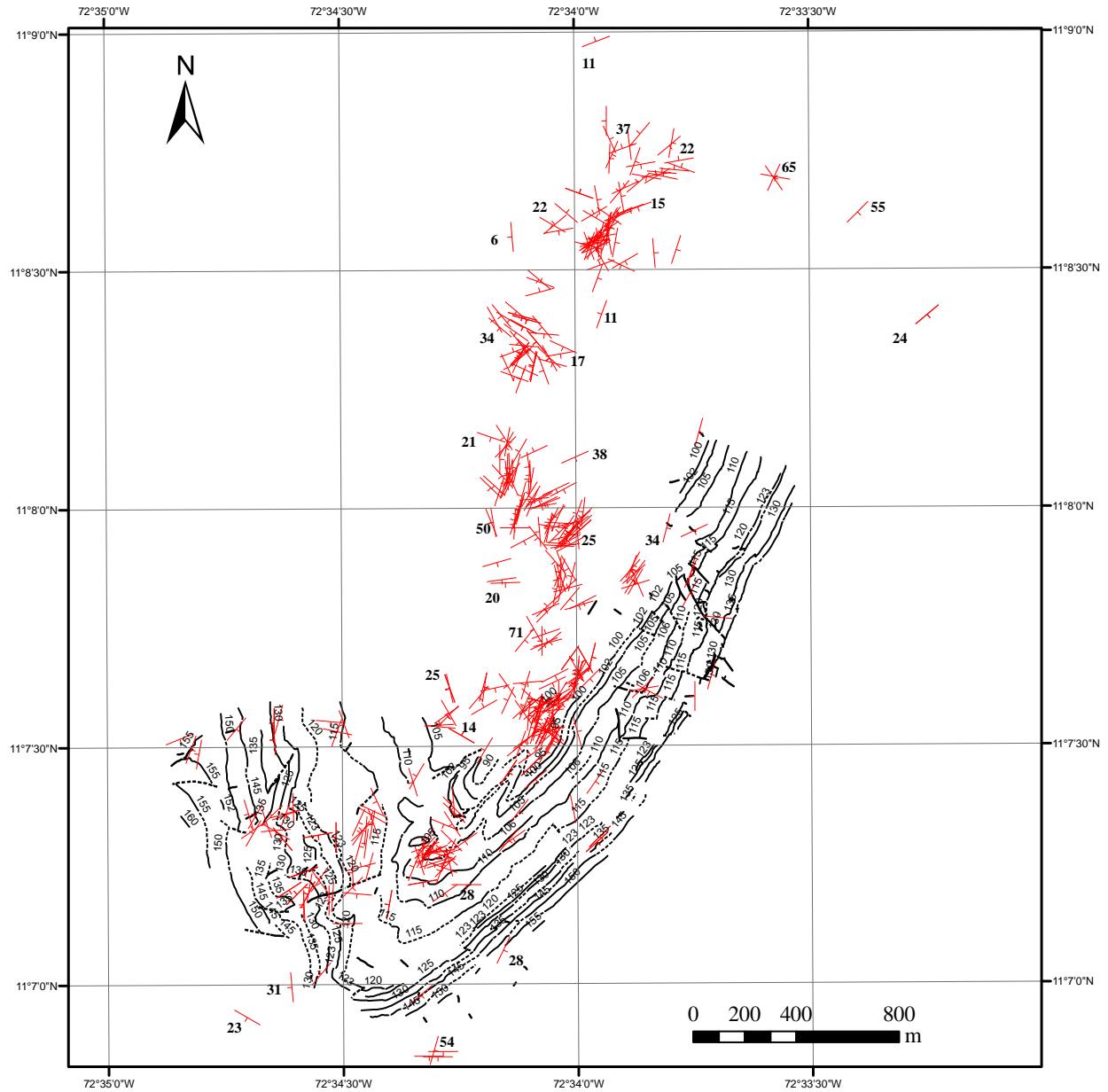


Figure 6. Map showing the location of bedding data (red strike and dip symbols) in the Tabaco anticline. Bedding data was measured in all mining levels. The black lines are the coal seams and faults traces in the lowest mining level 0. Numbers on coal seams traces are the coal seams ids. (data from Montes et al., in prep.).

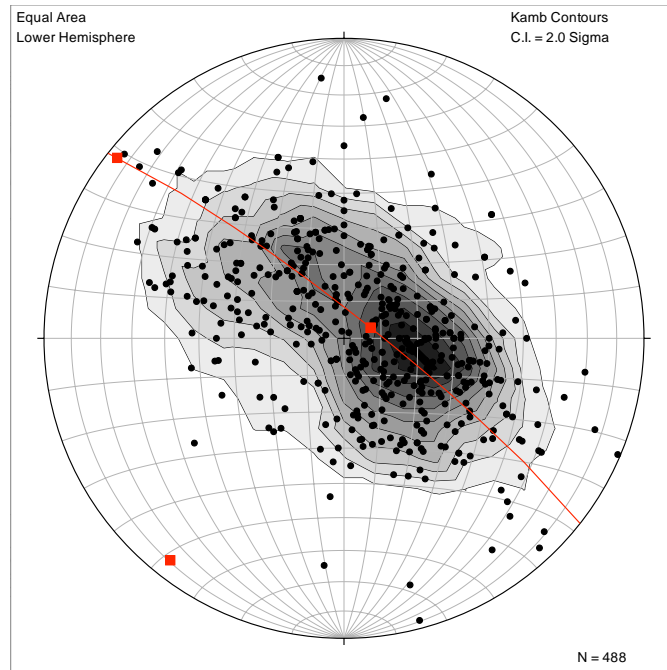


Figure 7. Lower hemisphere stereographic projection of poles to bedding in the Tabaco anticline. A cylindrical best fit to the data (red great circle and eigenvectors) suggests a fold axis of $217/7$.

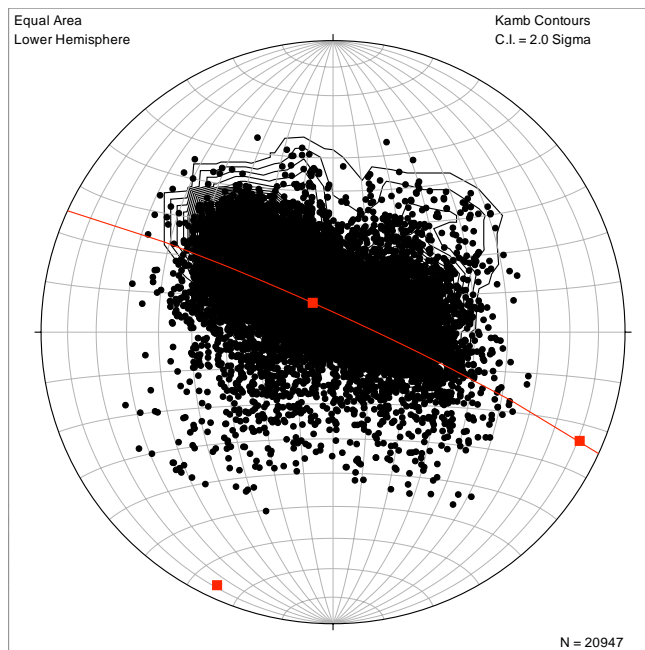


Figure 8. Lower hemisphere stereographic projection of poles to bedding from the reconstructed coal seams 3D surfaces. A cylindrical best fit to the data (red great circle and eigenvectors) suggests a fold axis of $204/5$.

A down-plunge projection of the coal seams along the fold axis 217/7 was performed (Allmendinger et al., 2012). Since the anticline is not perfectly cylindrical, not all points on a coal seam surface fall along the same line in the projection (Figure 9). However the down-plunge projection is still useful to visualize the geometry of the anticline. The projection shows that the anticline is asymmetric, with a SE vergence, and a rounded hinge. Lower points in the projection suggesting a west dipping, overturned forelimb, should not be taken into account. They result from projecting the entire data to the profile plane. Disharmonic folds, for instance in beds 100-105 and 150-155 towards the east, were observed in the anticline (cross section C-C in Figure 12). Small thickness changes are also observed between the coal seams.

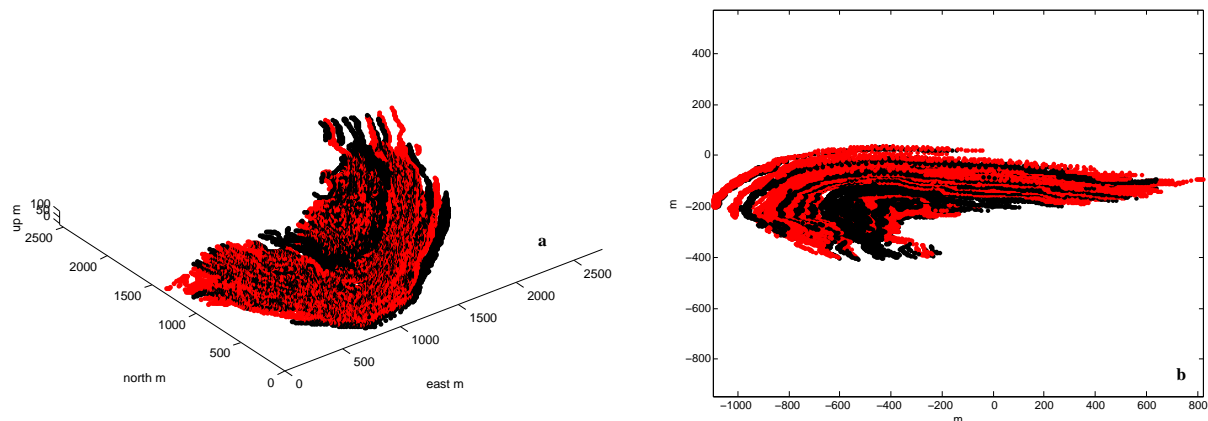


Figure 9. Down-plunge projection of the Tabaco anticline. a) 3D view of the anticline. b) Down-plunge projection of the anticline. Notice that since the fold axis plunges south (Figure 7), the cross section in b is looking to the south (east is to the left).

Based on the dataset above, detailed field mapping, and kinematic indicators; Palencia (2007) divides the anticline into four structural domains (Figure 5). 1) The Tabaco fault domain (DFTAB), characterized by a main SE dipping reverse fault (Tabaco fault) and a series of SE dipping, right-stepping in echelon reverse faults, the average dip of these faults is around 54° . 2) The Samán fault domain (DFSS) (left-lateral strike slip fault), characterized by short faults with high dip angles and striking NNW-SSE. 3) The Samán fault antithetic domain (DAFS), characterized by short segment faults with an average dip of 55° S-SW and NE with almost no

associated folding. And 4) The southeast limb domain (DFLSE), characterized by short segment faults with an average dip of 60° NE and SW. Additionally, the kinematic indicators (in the core of the anticline) suggest a tectonic transport direction to the northwest (between 310° and 330°) consistent with shortening perpendicular to the strike of the Cerrejón thrust, but in a direction opposite to the vergence of the Tabaco anticline.

3 Methods

3.1 Construction of 3D structural model

To describe and analyze the geometry of the anticline, a 3D structural model was built. The 3D model was important since it was a way to integrate the data on the different mining levels. When the coal seams and the fault planes were reconstructed, and the relationship between these two were checked, it was possible to evaluate the consistency of the model (whether the model was geologically reasonable or not). The 3D model was made in two steps: 1. Coal seams construction, and 2. Fault network construction.

3.1.1 Coal seams construction

Since the initial GIS project was the result of cleaning and interpretation of the original GPS data (Figure 10a, Montes et al., in prep.), the first step in the construction of the 3D model was the resampling of the coal seams and fault traces to increase the number of vertices on them. This was done by setting vertices every 2 meters along the traces, using a resampling tool in ArcGIS. This process did not change the shape of the traces, it just increased the number of vertices on them (Figure 10b).

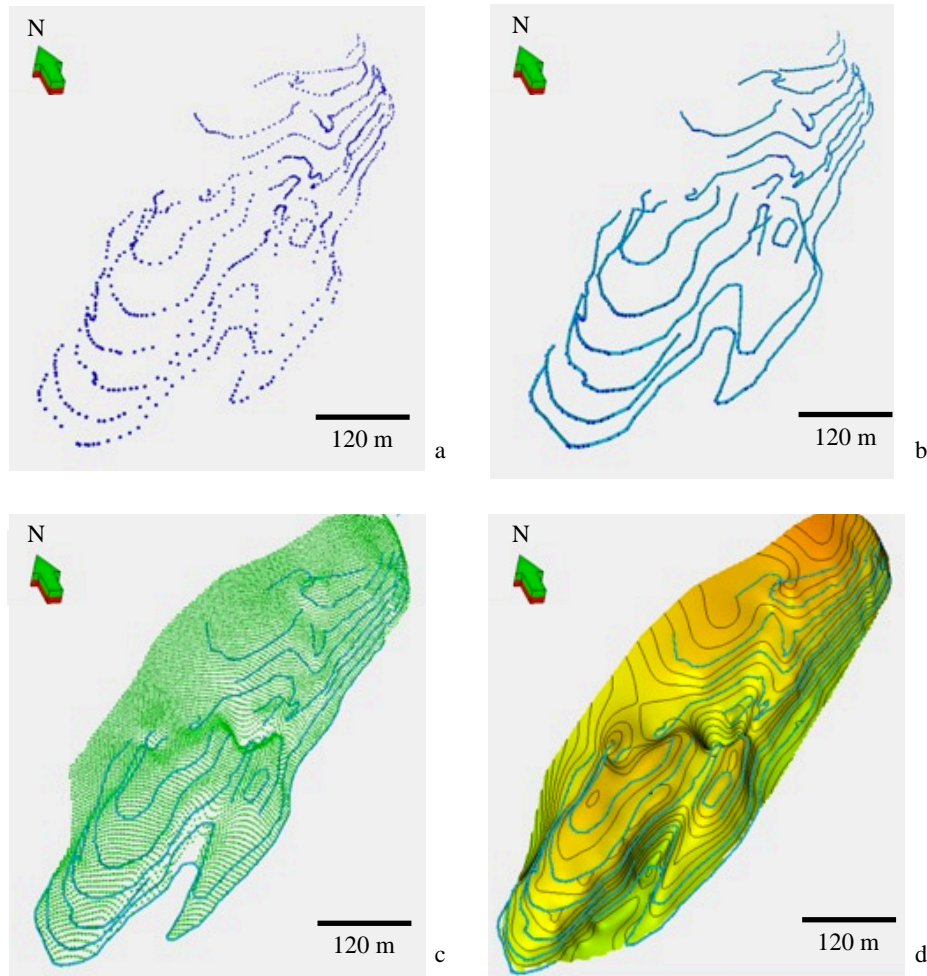


Figure 10. Steps in the construction of the coal seam surfaces, in this case coal seam 100. a) Original points. b) Resultant points (light blue) after resampling the original data (dark blue). c) Resultant points (green) after gridding. d) Final coal seam surface with contours. In c and d, the blue lines are the resampled data in b. Notice that the modeled surface closely follows the data.

Second, each coal seam was interpolated in Matlab using a grid fitting routine called gridfit (D’Errico, 2005). Gridfit fits a surface to scattered or regular 3D data points. It allows the existence of point replicates in x and y but with different elevation. Gridfit also allows building a gridded surface directly from the data, rather than interpolating a linear approximation to a surface from a Delaunay triangulation. A low smoothness was used in this process to closely follow the traces. Only interpolated areas with control data were exported. The purpose of this step was to increase the number and regularity of data points in the coal seam, while closely following the original data (Figure 10c-d). Steps 1 and 2 were performed to guarantee that the

coal seams were continuous enough. Near a fault scarp for instance, the coal seam must have enough resolution and continuity to create lines of intersection (cutoff lines) with the fault.

3.1.2 Fault network construction

The first step was to quality control and edit the fault traces, to make sure they follow the offsets displayed by the traces of the coal seams. The second and most crucial step was the correlation of the fault traces on the different mining levels (Figure 11a). This undoubtedly was the step with highest uncertainty and where it was possible to introduce interpretation errors. The traces were visually correlated level by level in Petrel (Figure 11a). Some of the challenges I faced were: Fault traces were mapped by different geologists with perhaps different connotations as to what a fault trace is. Where fault traces of similar strike were very close in a mining level, it was difficult to identify the correct trace to correlate. Another challenge was that in some areas one trace in one level looked as it could be correlated with another in a different level, but the strike of the traces were different, giving an irregular fault plane. The question here was whether to include or not the fault trace.

Each group of correlated fault traces were triangulated into a fault plane (Figure 11b). Some of the fault planes were very irregular (Figure 11b). To make a more geologically reasonable plane, an interpolation of the fault traces with a small degree of smoothing was made using gridfit (D'Errico, 2005). The result was a more regular fault plane that still followed the fault traces (Figure 11c). Finally a double check of the fault surfaces was made with the original fault traces and with the coal seams.

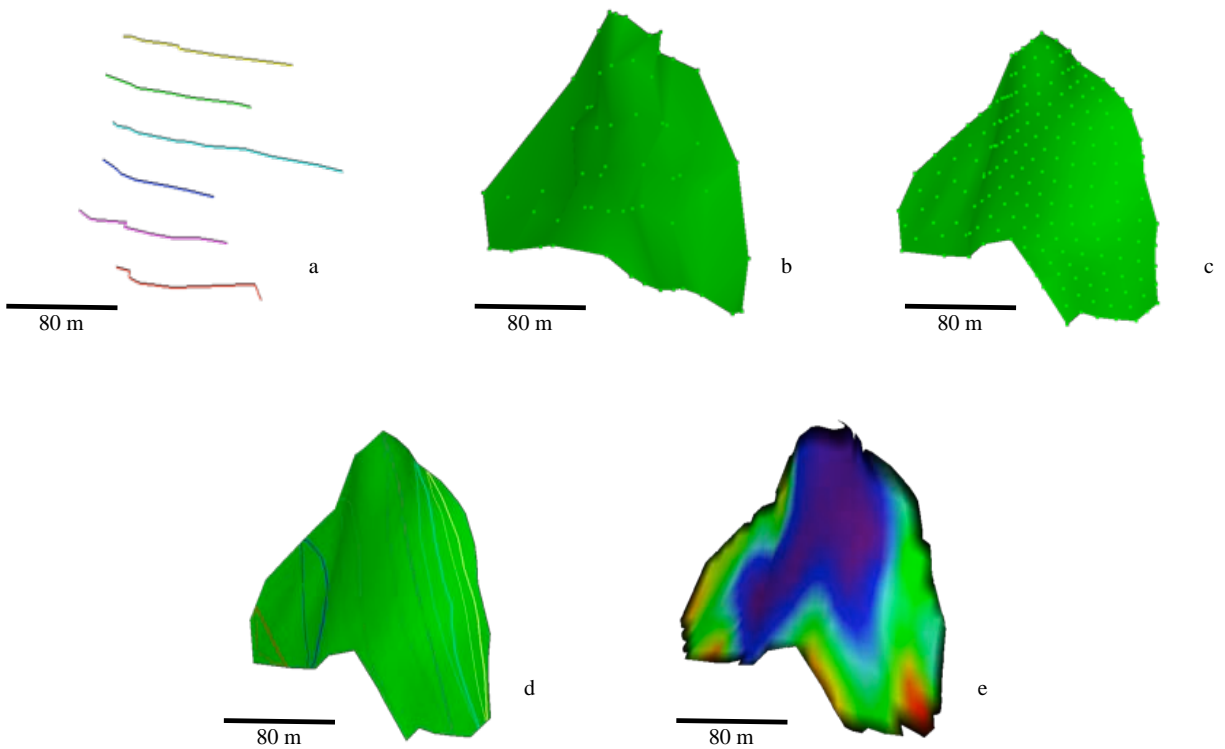


Figure 11. Steps in the construction of fault planes. a) Correlation of fault traces on different mining levels. b) Triangulation of fault traces to obtain a fault plane. c) Gridding of fault plane to obtain a more geologically reasonable structure. d) Computation of fault-coal seams intersections. e) Estimation of the throw attribute in the fault planes.

3.2 Fault displacement analysis

Fault displacement analysis was used in this thesis with three main objectives: 1) To check inconsistencies in the interpretation, 2) to understand the behavior of the fault network in the anticline in terms of displacement, and 3) to look at the fault displacement gradients or fault-related strains.

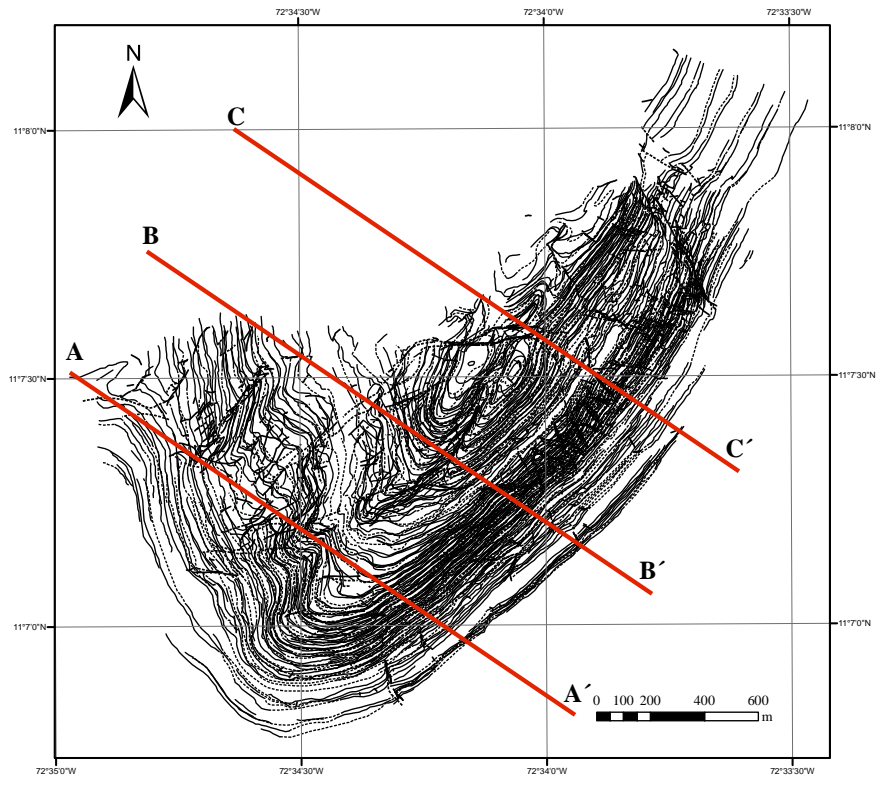
The first step was to calculate in TrapTester the faults-coal seams intersections. This process generated a series of polygons that represent the hanging wall and footwall cutoffs (Figure 11d). The input for this step were the fault planes and the coal seams of the 3D structural model. I only worked in areas with control data, so in the case of the younger coal seams, fault-horizons intersections were not computed in the core of the anticline (Figure 12).

Some of the faults-horizons intersections polygons show anomalies (for example abrupt spikes). After checking the consistency of the modeled coal seams and fault planes, and if these irregularities persist, a minor edition of the faults-horizons intersection polygons was performed. Then the throw attribute was computed on the fault planes (Figure 11e). The throw on the fault surface is derived from the cutoffs generated in the fault-horizons intersection step. With the 3D model and the throw information, fault statistics were calculated, including fault orientation plots, fault displacement profiles, and fault array summation and strain. This was done using the fault statistics tool of TrapTester.

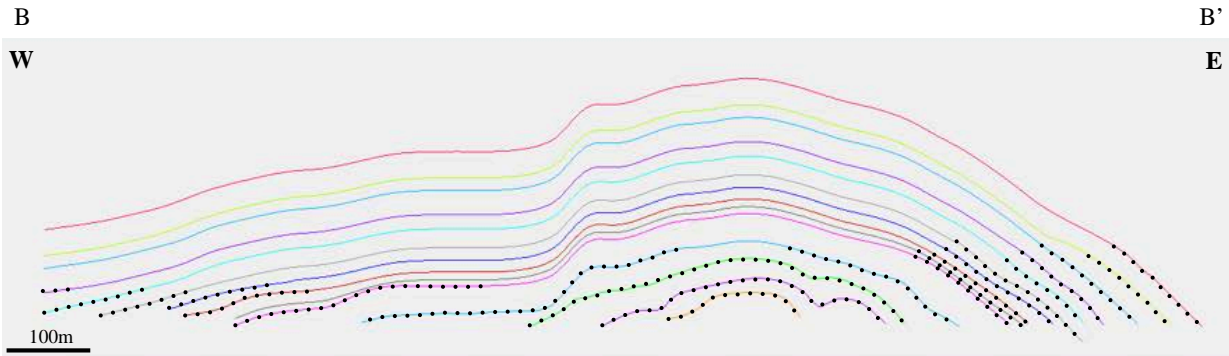
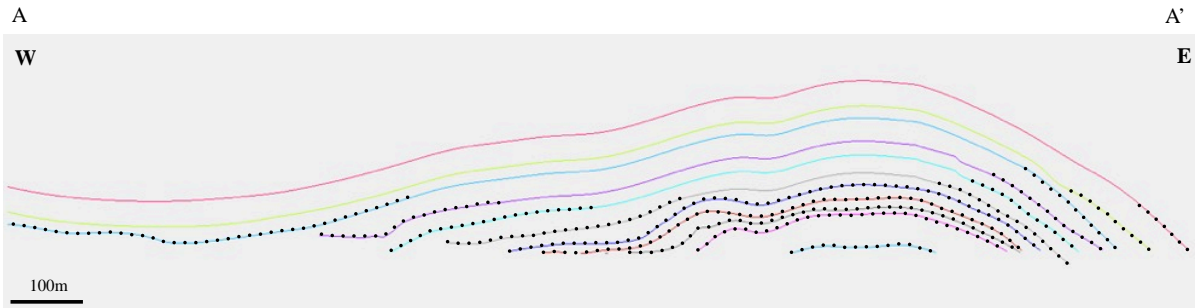
3.3 Restoration of the anticline

To restore the anticline, the coal seams data and the fault surfaces were imported into 3DMove. In the case of the coal seams, I reconstructed the part of the anticline without data. This applies mostly to the younger coal seams without data in the core of the anticline (Figure 12). To avoid errors in the reconstruction of the surfaces, for instance crossing of surfaces in the core of the anticline, the area without control data was reconstructed from the older surface assuming parallel folding or constant stratigraphic thickness across the structure (Figure 12). This assumption is not completely correct because as we can see in the cross sections in the area with control data (black dots), the beds are not completely parallel (Figure 12). However, this is a reasonable approach to represent the core of the anticline in younger levels.

After reconstructing the coals seams, a kinematic restoration of the anticline was performed using a 3D flexural-slip restoration technique in 3DMove. This technique utilizes a slip method that preserves volume in 3D, line length in a given unfolding direction, and orthogonal bed thickness (Griffiths et al., 2002). The technique only deals with the coal seams and does not take into account the slip on the fault surfaces (that would be very hard to do with so many fault surfaces). My aim is to compare the kinematics and strain of this “unfolding” restoration with those obtained in the fault displacement analysis of the previous section.



a



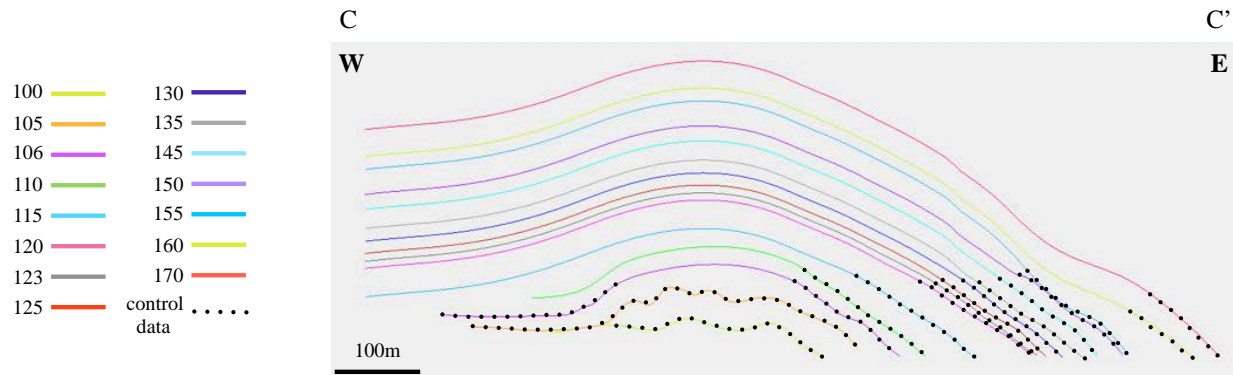


Figure 12. a) Map showing the location of cross sections A-A', B-B' and C-C'. These cross sections are shown after the reconstruction of the younger coal seams with parallel folding. Black dots in the sections show the areas with data. Sections have no vertical exaggeration. Numbers on legend refer to the coal seams IDs.

3.4 Curvature

The curvature of the coal seams was calculated using differential geometry algorithms by Mynatt et al, (2007). The Matlab codes for the calculations were taken from Pollard and Fletcher (2005, their chapter 3). The principal curvatures, k_{\max} and k_{\min} , were calculated, as well as the geological curvature. The geological curvature is based on the gaussian curvature ($k_G = k_{\min} * k_{\max}$) and the mean curvature ($k_M = (k_{\min} + k_{\max})/2$) (Mynatt et al., 2007). The geologic curvature defines the shape and orientation of points on the folded surface. The curvature threshold specifies an absolute curvature value below which calculated principal curvatures are set to zero, thereby allowing the classification of “idealized” shapes (Bergbauer, 2002). Figure 13 shows the geologic curvature classification scheme for points on a surface as a function of the Mean and Gaussian curvatures (Mynatt et al, 2007).

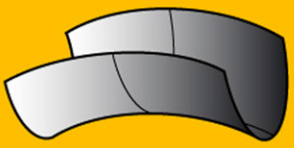
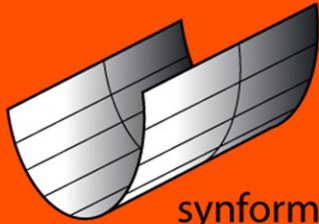


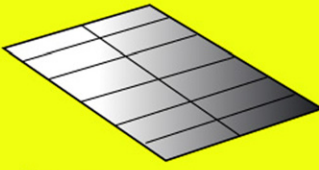
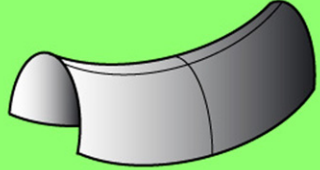
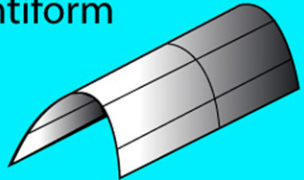
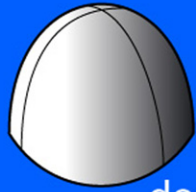
	$k_G < 0$	$k_G = 0$	$k_G > 0$
$k_M < 0$	 synformal saddle	 synform	 basin
$k_M = 0$	 perfect saddle	 plane	
$k_M > 0$	 antiformal saddle	 antiform	 dome

Figure 13. Geologic curvature classification. The geologic curvature of a point on a surface can be determined from the gaussian (k_G) and mean k_M curvatures. The color code is used in the curvature calculation (Mynatt et al., 2007).

4. Results

4.1 3D structure of the Tabaco anticline

4.1.1 Fault geometry:

Figure 14 shows the faults in the 3D structural model. A total of 67 faults labeled 1 to 67, were interpreted in 17 coal seams. Most of the faults are reverse, except fault 45 (Samán fault), which is as a left lateral strike-slip fault (Palencia, 2007). Only faults displacing more than one coal seam are present in the 3D model. Rose diagrams of fault orientations are also included in Figure 14.

The four fault domains mapped by Palencia (2007) in the field, were identified in the 3D model (Figure 14). The four domains are: 1) The Tabaco fault domain (DFTAB) which is present in the anticline's S-SW limb. In the 3D model, the faults belonging to this domain are long (300-400 m along strike) reverse faults with a strike NE-SW (except for fault 59 that has an E-W strike). 2) The domain of the SE limb (DFLSE). The faults belonging to this domain are mainly short (100 to 150 m along strike), except for fault 1 (340 m along strike). Their strike is NW-SE and approximately E-W to the south of the anticline. Between coal seams 120 and 145, some of the faults show a conjugated pattern. 3) The antithetic Samán fault domain (DAFS). The faults belonging to this domain are very short segments (60 m along strike) close to the Samán fault. These faults get longer as their distance to the Samán fault increases (for instance fault 63 is 340 m along strike, Figure 14 coal seam 123). The strike of the faults in this domain is NW-SE. 4) The Samán fault domain (DFSS) which consists of the Samán fault and a couple of very short faults (50 m along strike). In the original database (Figure 5) there were more fault traces belonging to this domain. However, these faults offset just one coal seam and therefore were not included in the 3D model.

Coal seam 95 is affected by 4 main faults with a main orientation NW-SE (Figure 14). These faults are located in the eastern limb of the anticline, and belong to the fault domains DFLSE, DFTAB, and DAFS. Coal seam 100 is affected by 7 main faults with a main orientation NW-SE (Figure 14). These faults are mainly located in the eastern limb of the anticline. In addition, fault 59 crosses almost the whole seam in an E-W direction (Figure 14). The faults affecting this coal seam belong to the domains DFLSE, DFTAB, and DAFS.

Coal seam 102 is affected by 6 main faults with a main orientation NW-SE (Figure 14). Almost all the faults that offset this coal seam are the same as those of the lower coal seam 100, except fault 60 which has a different strike NE-SW, and it is located in the SW part of the anticline. Additionally fault 45 (the Samán fault) was identified in this coal seam. The faults affecting this coal seam belong to the domains DFLSE, DFTAB, DAFS and DFSS. Coal seam 105 is affected

by 7 main faults with two main orientations, NW-SE which are located in the NE limb of the anticline, and NE-SW which are located to the south of the anticline. The faults in the south with a strike NE-SW belong to the domain DFTAB, and those striking NW-SE belong to the domains DFLSE, DAFS and DFSS.

Coal seam 106 is affected by 6 main faults with orientations similar to those in the lower seam 105. The NW-SE striking faults are located in the NE limb of the anticline, and the NE-SW striking faults are located to the south of the anticline. In this coal seam (and the seams above), there are no data from the core of the anticline, so there is no control for the faults affecting this part of the anticline. Therefore it is not possible to know the behavior of faults such as fault 59 in younger coal seams. The faults in the south with a strike NE-SW belong to the domain DFTAB, and those in the NE limb with a strike NW-SE belong to to the domains DFLSE, DAFS and DFSS.

Coal seams 110 and 115 are affected by 15 and 16 main faults respectively, with strike NW-SE in the NE limb, NE-SW in the south, and a new fault, fault 1, striking E-W. In these coal seams, the number of faults with strike NE-SW increases. The faults in the south with strike NE-SW belong to the domain DFTAB and the faults in the NE with strike NW-SE belong to to the domains DFLSE, DAFS and DFSS. Fault 1 (E-W) also belongs to the domain DFLSE.

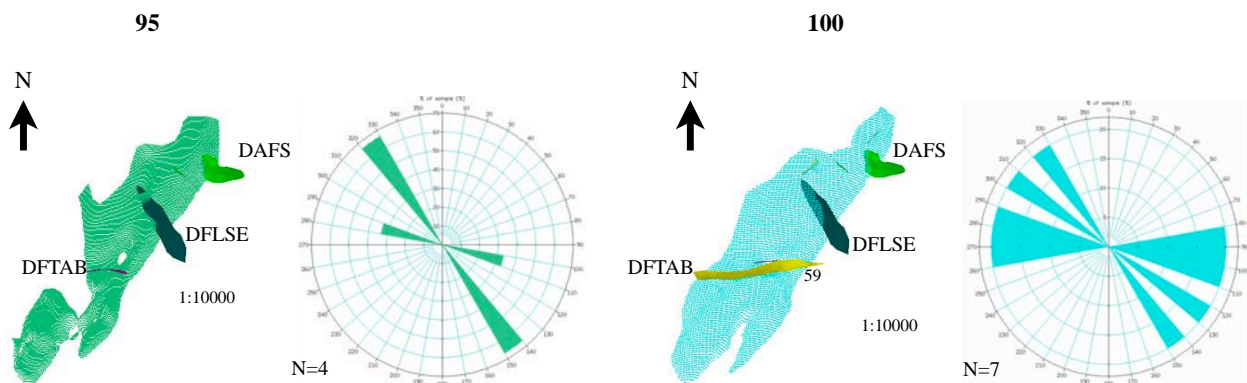
Coal seam 120 is affected by 22 faults with strike NW-SE in the NE limb, NE-SW in the south, and fault 1, striking E-W. In this coal seam, a conjugated pattern of the faults in the eastern limb was recognized. This conjugated pattern include two orientation of thrust faults and it was very clear in coal seams 120 to 145. The faults that show the conjugated pattern belong to the DFLSE domain. The other 3 domains were also recognized here.

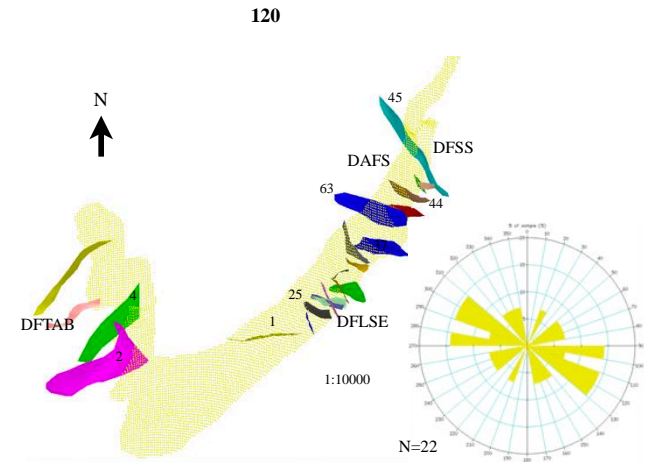
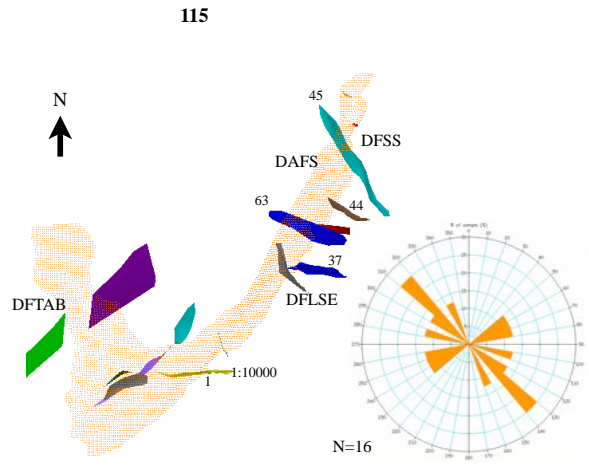
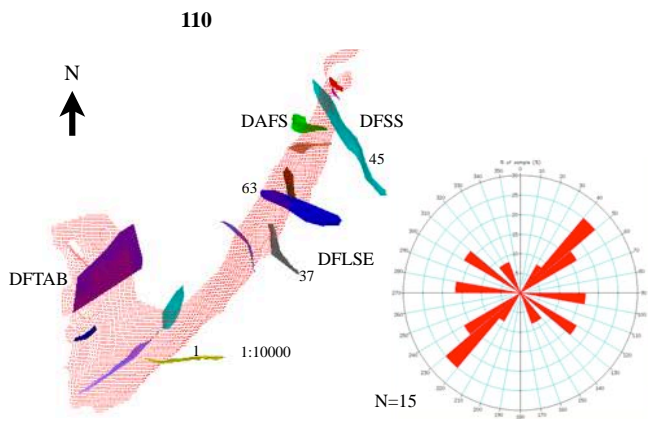
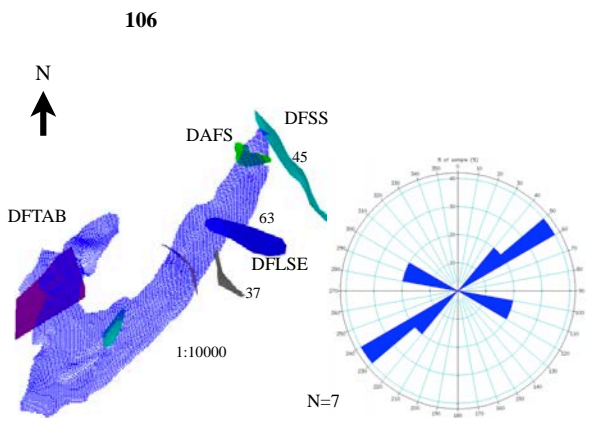
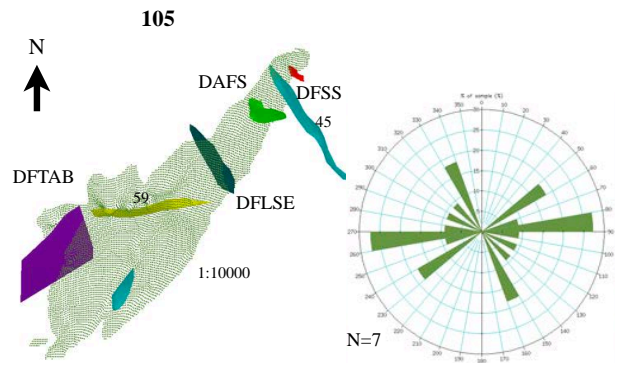
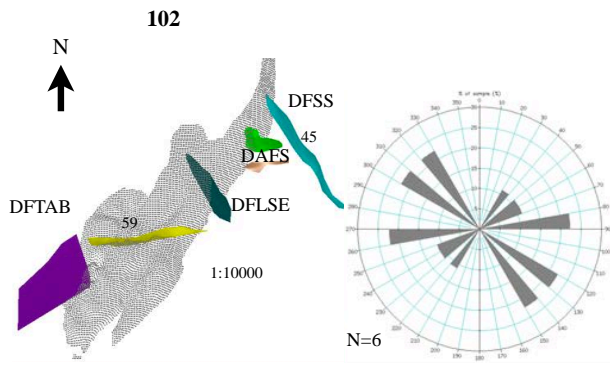
Coal seams 123, 125, 130, 135 and 145 are affected by 25, 29, 29, 28 and 25 faults respectively, with strike NW-SE in the NE, NE-SW in the SW, and E-W in the SE. One characteristic of these coal seams is that they have a series of E-W faults in the southern part of the anticline.

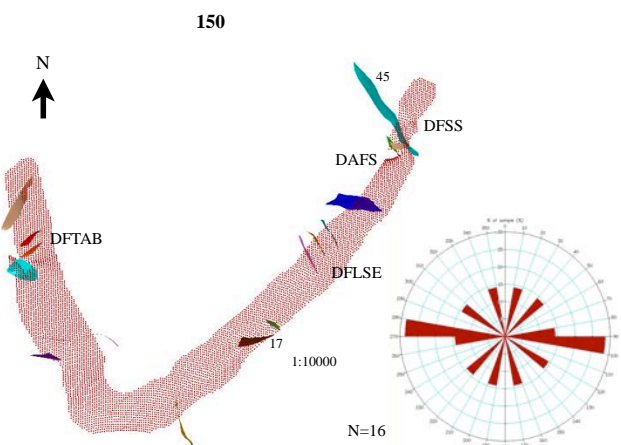
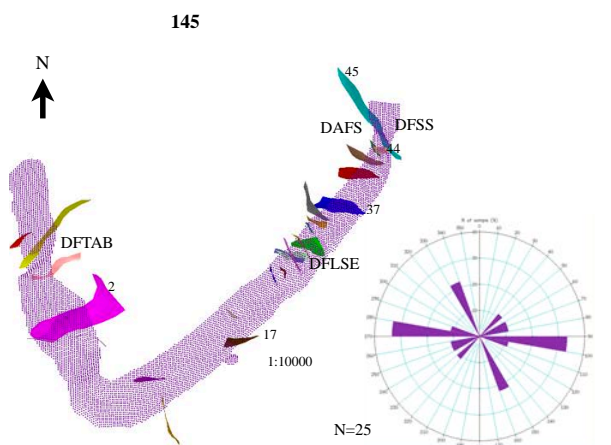
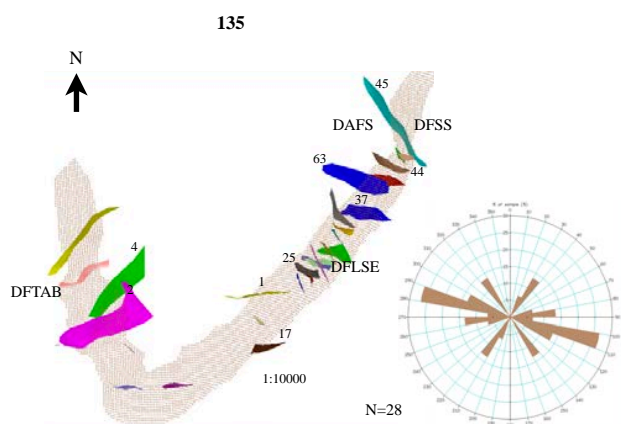
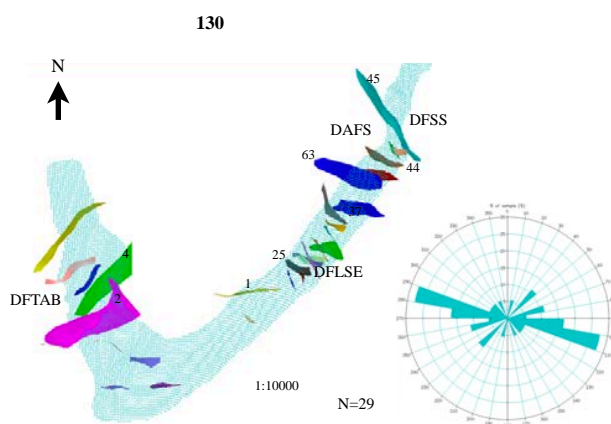
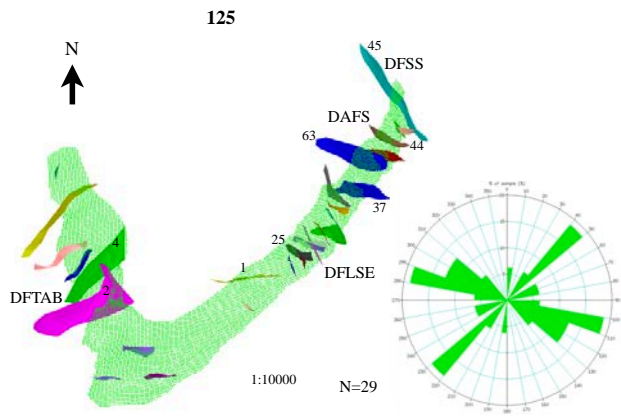
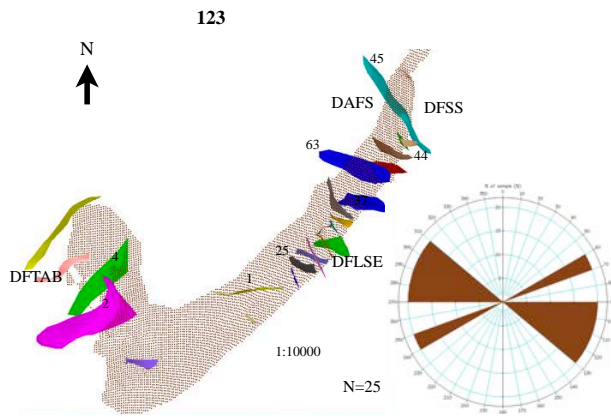
Additionally the conjugated pattern in the east limb is also present. Both the E-W faults and the conjugated pattern belong to the DFLSE domain. The other 3 domains were also recognized here.

In coal seam 150 the number of faults start to decrease. This coal seam is affected by 16 faults with two main strikes, NW-SE and NE-SW. Faults striking E-W have almost disappeared. In this coal seam the conjugated pattern was not observed. This is the last coal seam where the 4 faults domains were observed. Coal seam 155 is affected by 12 faults with two strikes, NW-SE and NE-SW. In this coal seam, there was not a lot of information available in the north part of the anticline, so only 2 domains were recognized, DFLSE and DFTAB.

Coal seam 160 is affected by 8 faults with a main strike NW-SE. In this coal seam there are only faults in the eastern limb that belong to the DFLSE, DAFS and DFSS domains. The last modeled coal seam, 170, is affected by 4 faults with a main strike NW-SE in the SE. The faults affecting this coal seam belong to the DFLSE domain.







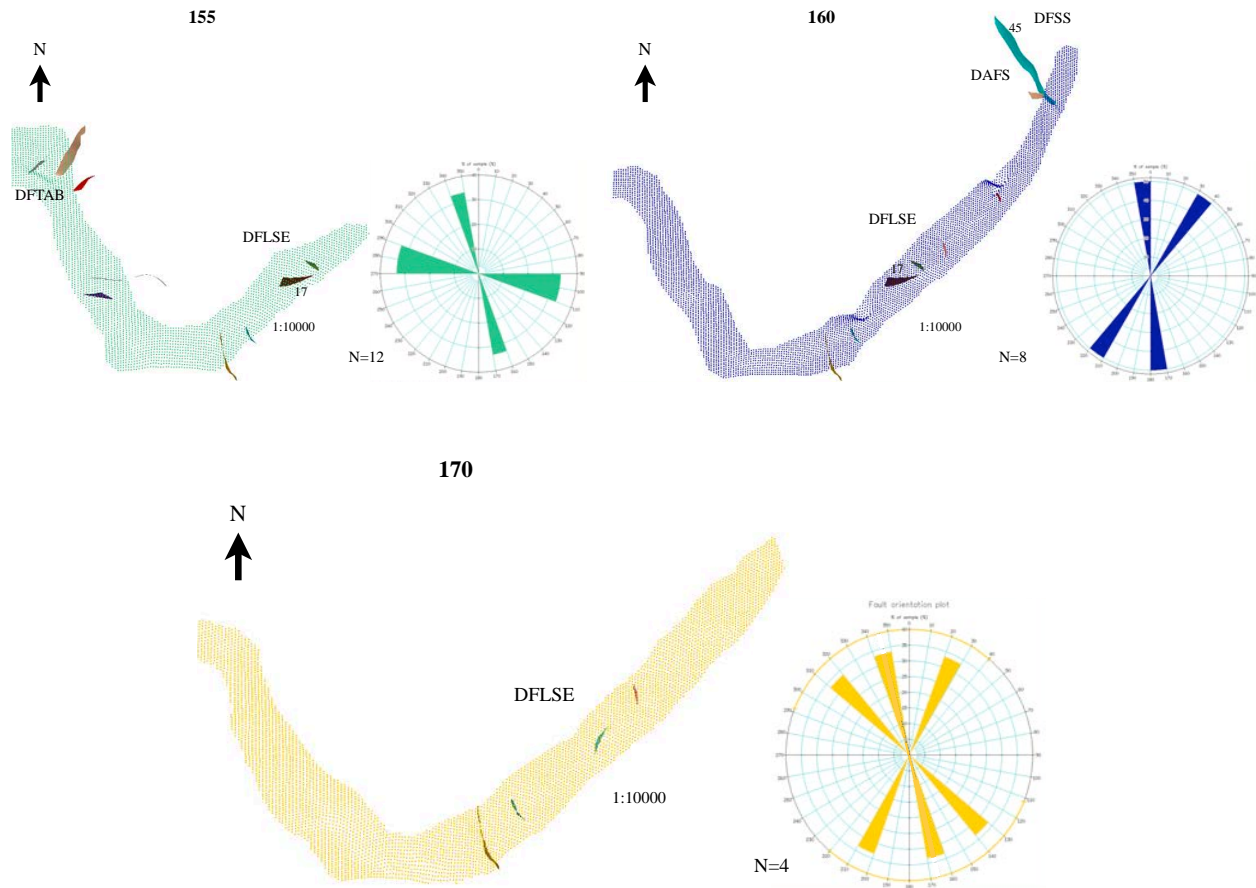


Figure 14. Faults in the 3D model and their occurrence in each of the coal seams. Faults are labeled with number 1 to 67. Numbers on top of the figures refers to the coal seam (95 is the lowest coal seam). Rose diagrams show the orientation of the faults in each coal seam. N is the number of faults. DFTAB : Tabaco fault domain, DFLSE: Southern limb domain, DAFS: Samán fault antithetic domain, and DFSS: Samán fault domain.

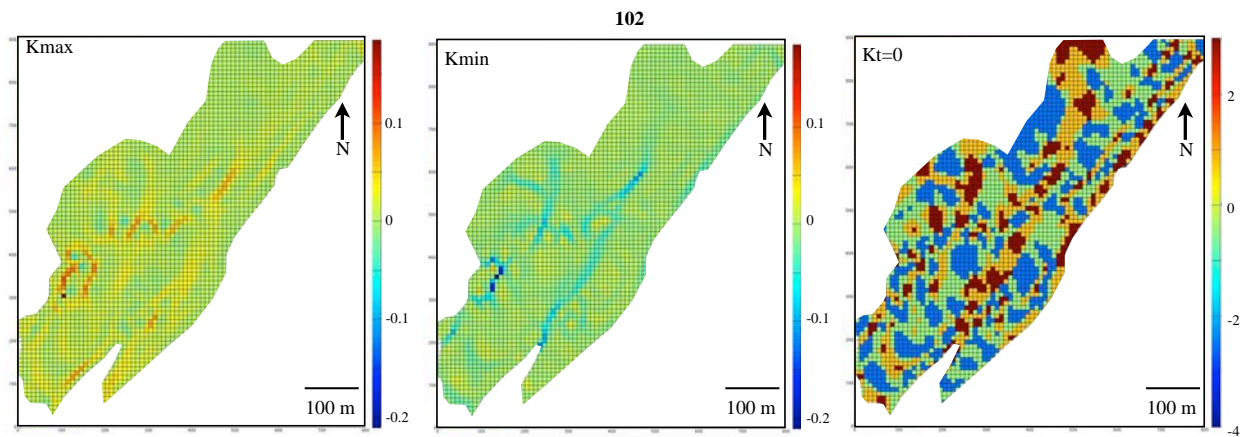
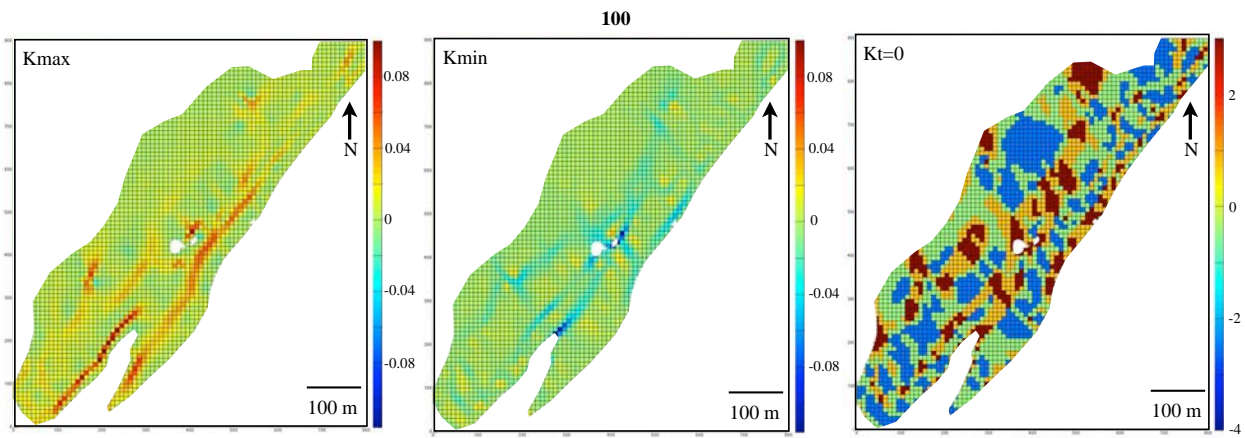
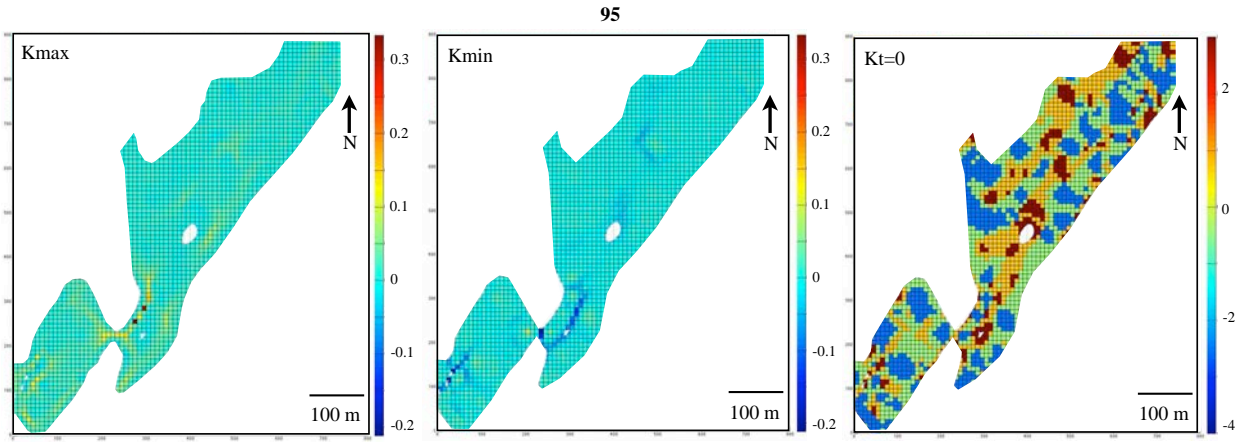
4.1.2 Curvature:

Curvature was calculated in the older, more complete stratigraphic seams (95, 100, 102, 105, 106). Curvature was also calculated in coal seam 130, which has the highest amount of faults. Figure 15 shows the maximum curvature (k_{max} , left side), minimum curvature (k_{min} , middle side) and geologic curvature (right side).

k_{\max} highlights the anticline's hinge and minor folds hinges. The anticline's hinge is clearly visible in coal seam 100 suggesting a fold axis trending 210° (approximately the same as in Figures 7 and 8). In the other coal seams, the highest values of k_{\max} indicate minor hinges. k_{\min} mainly highlights synclines but also erosional features (drainage pattern). The principal curvatures clearly show that the fold is no cylindrical. A folded surface is cylindrical when the principal curvature parallel to the hinge line is zero (Mynatt et al., 2007).

By using the concept of geologic curvature and implementing a curvature threshold (k_t), it is possible to examine how far a coal seam departs from the cylindrical geometry (Mynatt et al., 2007). Figure 15 (right side) shows the geologic curvature calculated across the surface with $k_t = 0$. The color code of Figure 13 is used in the coal seams. The geologic curvature calculated across the surface with $k_t = 0$ shows that no principal curvatures are approximated as zero, so no cylindrical or planar points appear. As it can be seen, there are no orange, yellow or light blue colors representing cylindrical synforms, planes or antiforms (Figures 13 and 15 right side). Areas on the surface are identified as domes, basins, and antiformal and synformal saddles. The domes (blue) and the antiformal saddle (green) coincide with the anticlinal hinge, and the basin (dark red) and synformal saddles (dark yellow) coincide with the synclines position or valleys (Figure 15).

In coal seam 130 there is a clear difference between the size of the basins (dark red) and synformal saddles (dark yellow), in both limbs. In the western limb the basins are bigger than in those in the eastern limb (Figure 15 right side). For this coal seam the eastern limb of the anticline is affected by more faults than the western limb (Figure 14).



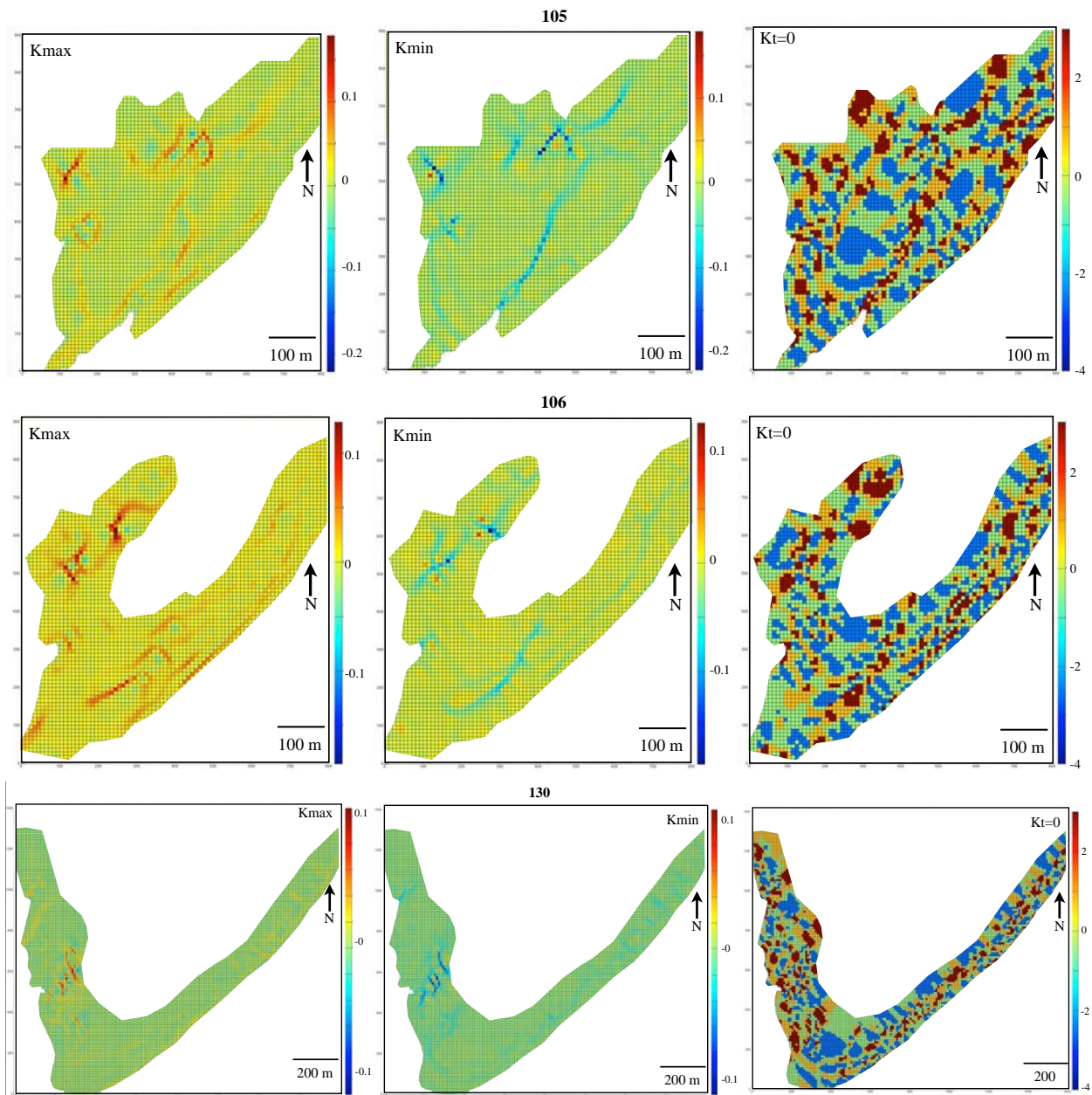


Figure 15. Distribution of maximum curvature (k_{max}), minimum curvature (k_{min}) and geologic curvature with $k_t = 0$. Curvature was calculated for coal seam 95, 100, 105, 106 and 130.

4.2 Fault displacement analysis

4.2.1 Fault displacement patterns

The throw was calculated for all faults in the 3D model. Figure 16 shows four different fault throw patterns: 1) Low throw in the middle of the fault and high throw in the areas around (Figure 16a), 2) Highest throw at one corner of the fault and not in the center (Figure 16b), 3) the most common pattern, highest throw in the middle of the fault (Figure 16c), and 4) In conjugated faults, the highest value of throw is located at the intersection of the two faults (Figure 16d).

Figure 16a shows a fault plane with low throw in the middle of the fault and high throw in the areas around. This pattern was observed in two faults of the model. Three possible explanations for this pattern are: 1) the area of low throw suggests a tip point which indicates that the mapped fault is actually 2 faults, so the fault plane should be split. 2) The linkage fault model (Peacock and Sanderson, 1991; Cartwright et al., 1995), in which the faults grew as isolated faults at early stages and linked to produce additional fault length. In this case the area of low throw is the region of fault linkage. 3) Outer areas of high displacement result from the intersection of two faults with different orientations that together add to a larger displacement (Kim and Sanderson, 2005). This third option is discarded because there are no other fault crossing the fault plane. However, it is difficult to know which of the two first options is generating this fault throw pattern.

Figure 16b shows the highest throw value in a corner of the fault and not in the center as we would expect (Figure 3). Two possible explanations for this pattern are: 1) the fault could actually be larger, but there are not enough data to cover the complete fault plane. 2) there is a problem in the interpretation of the faults.

Figure 16c shows two fault planes with the area of high throw in the middle of the fault. This is the most common pattern in the faults of the 3D model. Although this is not exactly the ideal

pattern of Figure 4, it is a consistent pattern of fault displacement. Figure 16d shows a pair of conjugated faults, where the highest value of throw is at the intersection of the two fault planes. The two faults with different orientations add to a larger displacement.

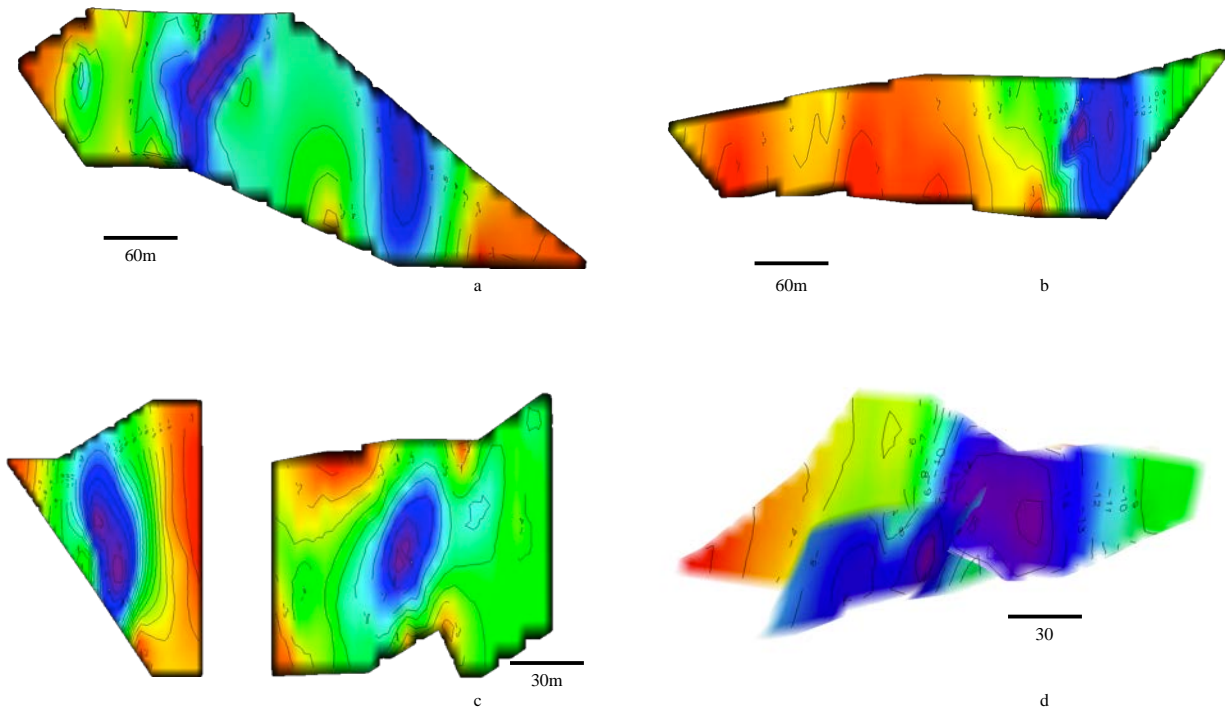


Figure 16. Fault throw patterns observed in the 3D model. The blue-purple color indicates the highest values of throw a) fault plane with low throw in the middle of the fault b) fault plane with highest throw at the corner of the fault c) fault planes with the highest throw in the middle of the fault d) fault throw in conjugated faults.

Figure 17 shows the distribution of the four displacement patterns in coal seam 130. This coal seam has the highest number of faults, so the distribution of the patterns here reflects very well the behavior in the anticline. Figure 17 shows that pattern 3 (P3) is the most common pattern, followed by pattern 2 (P2). Pattern 1 (P1) was observed in two faults in the anticline, and pattern 4 (P4) in conjugated faults.

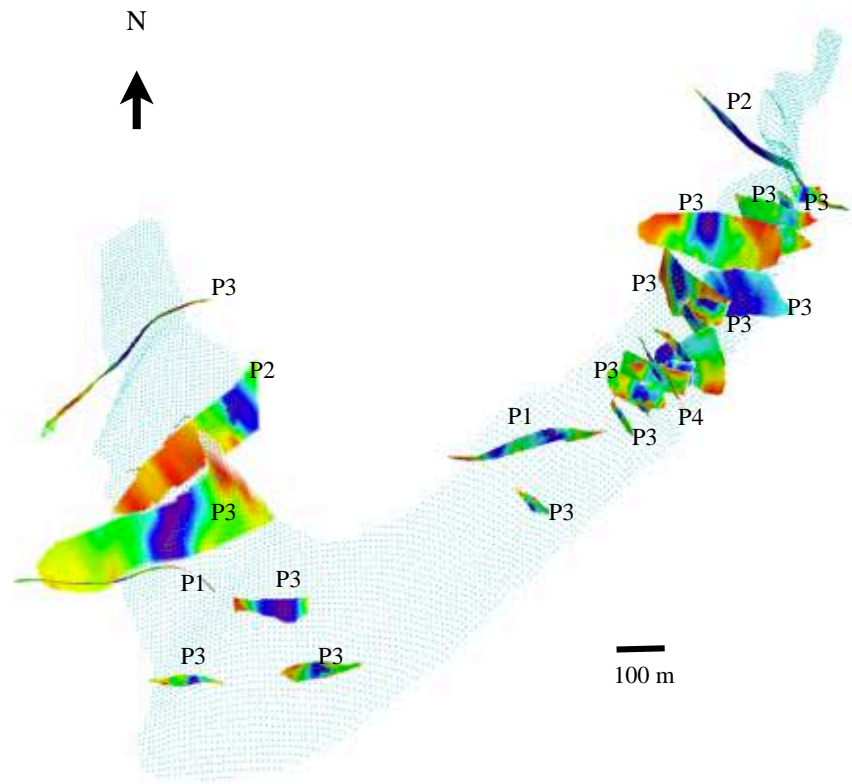


Figure 17. Distribution of fault displacement patterns (P1 to P4) in coal seam 130.

4.2.2 Fault array summation and strain

A series of fault displacement versus distance profiles were made for each coal seam in the anticline. Figures 18a-q contain maps showing the faults affecting each coal seam contoured by their throw attribute (left side), and plots of individual displacement, fault array displacement summation, and strain. The throw was measured along sample lines oriented perpendicular to the average strike of the faults. Sample line spacing (in the horizontal) was 10 m. The location of the sample grid was adjusted for each coal seam according to the area where the faults were located. That allows sampling and visualization of specific details in each case. The initial and the last position of the sampling line are shown in the map views of Figure 18.

Figures 18e-o for coal seams 106 to 155 show faults with two main strikes, NW-SE and NE-SW. For this reason two different plots of fault array summation and calculated strain (labeled 1 and 2) were made. The first one is for the faults with strike NW-SE (in the map view the area surrounded by the square **1**). The second one is for the faults with strike NE-SW (in the map view the area surrounded by the square **2**). In both cases the sample line spacing was 10 m.

The fault displacement versus distance profiles (Figure 18, middle and right side) show the vertical offsets (throws), the fault array summation, and the strain for the 67 interpreted faults in the 17 coal seams of the 3D model. The fault that shows a highest apparent throw is fault 59, which shows a throw of 21 m in coal seam 100, 27 m in coal seam 102, and 35 m in coal seam 105 (Figures 18b, c, and d). It is not possible to know the behavior of fault 59 in younger coal seams, due to lack of data in the core of the anticline.

Fault 45 (Samán fault) shows also an important amount of displacement (25 to 26 m in coal seams 105 and 110, Figures 18d and f). However, there is some uncertainty in the calculation of throw of fault 45 due to lack of data in some coal seams. Other faults that show an important amount of displacement are fault 63 in coal seam 115 (19 m, Figure 18g), fault 17 in coal seam 155 (18 m, Figure 18o), fault 25 in coal seam 130 (18 m, Figure 18k), fault 44 in coal seam 120 and 123 (17 m, Figures 18h and i), fault 37 in coal seam 120 (17 m, Figure 18h), fault 4 in coal seams 120 and 123 (17 m, Figures 18h and i), and fault 2 in coal seam 130 (16 m, Figure 18k).

On each coal seam, the aggregate vertical component of displacement (dashed line) was also calculated. For this analysis it is important to mention that the younger coal seams did not have any data in the core of the anticline. This can result in underestimation of cumulative throw in these younger seams. The coal seam with the highest value of cumulative throw (50 m) is 105, followed by coal seams 130 (44 m), and 125 (43 m) (Figures 18d, 18k and 18j). Coal seam 105 is affected by a limited number of faults (7 in total), so the high cumulative throw in this coal seam is due mainly to faults 59 and 45 (Figure 18d). In contrast, coal seams 125 and 130 are the ones affected by more faults (29 faults in both coal seams), so in these two cases the highest value of

the total throw results from the contribution of small throw faults (Figures 18j and 18k). In younger coal seams than 130, the total throw starts to decrease gradually up-section. Coal seam 135 shows a maximum cumulative throw of 29 m, 145 a maximum of 27 m, 150 a maximum of 15 m, 155 a maximum of 21 m, 160 a maximum of 12 m, and 170 a maximum of 15 m (Figures 18l to 18q).

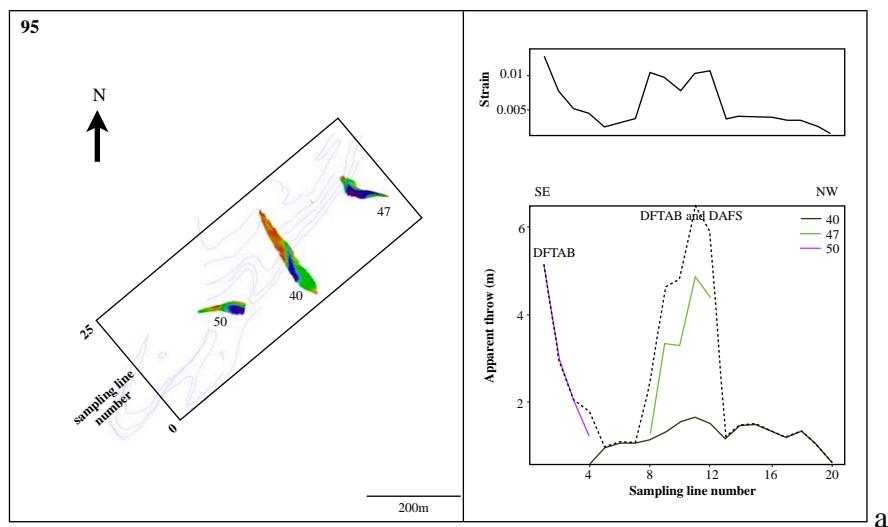
In some of the coal seams, it is easy to correlate the spikes in the cumulative throw curve with the different fault domains of Palencia (2007). Between coal seams 120 to 145 (Figures 18h and m), it is possible to identify 3 clear spikes. The first one corresponds to the cumulative throw generated by the conjugated faults of the DFLSE domain. The second spike is generated by the DFLSE domain (the no conjugated faults), but in some cases there are also faults of the DAFS domain. The third spike is generated by the faults that belong to the DAFS domain. The magnitude of these spikes changes through the coal seams. In coal seams 120 and 123 the highest spike is the third one, which includes the DAFS domain, with a throw of 30 m (Figures 18h and 18i). However, in coal seams 125 to 135, the highest spike is the first one, which belongs to the conjugated faults of the DFLSE domain, with the highest value of throw of 45 m (Figures 18j and 18k).

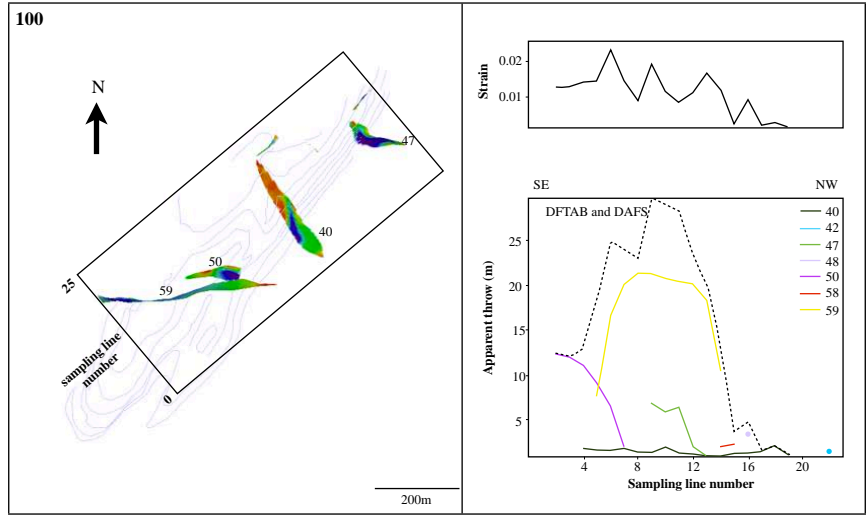
The spike generated by the domain DFSS is more difficult to see due to the lack of data in the coal seams in the most northern part of the anticline. However this pattern is clearly indicated in coal seam 125 (Figure 18j). The pattern of the DFTAB is mainly shown on the right side of Figure 18. However, in half of the cases the cumulative throw curve does not resemble a continuous curve due to the faults being widely spaced. In general, it is not possible to observe that the displacement in the anticline gradually decreases towards one specific direction, but it seems to decrease up-section younger coal seams than 130 as indicated before.

Figure 18 also shows the fault-related strain (i.e. horizontal elongation calculated from aggregate heave of all faults divided by original length of horizon) for each coal seam over the 3D model. The fault-strain in the modeled coal seams of the anticline varies between 0.0015 in coal seam

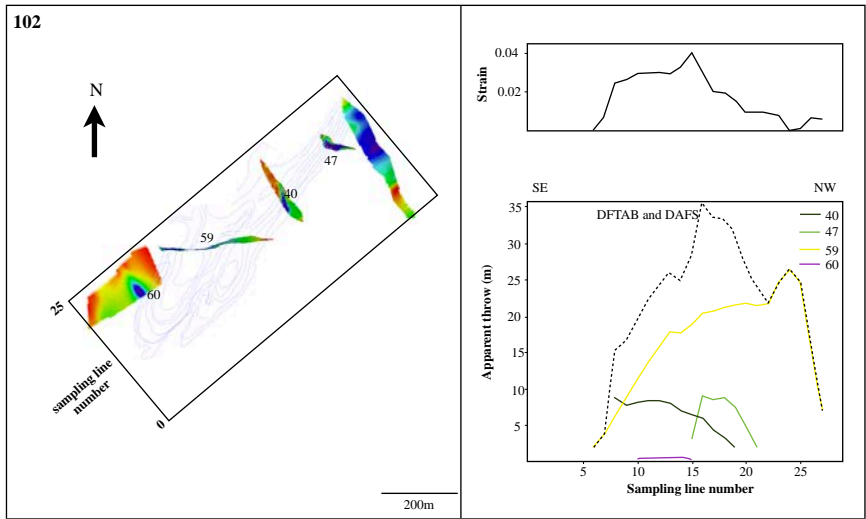
150, and 0.2 in coal seam 123 (Figures 18n and 18i). Only coal seam 123 shows strain values higher than 0.1, while coal seam 105 has values of 0.1 (Figures 18i and 18d). Freeman et al. (2010) based on a large number of published data for strike dimension and maximum displacement for faults, established that 0.1 represents a realistic upper limit of the longitudinal strain when it is measured in the displacement direction of a fault. The strain value 0.2 identified in coal seam 123 (Figure 18i, right side) is higher than the upper limit suggested by Freeman et al. (2010). This value of 0.2 is generated by fault 4 (Figure 18i, right side). Additionally to the high value of fault-related strain, fault 4 has the second fault throw pattern: fault plane with highest throw at the corner of the fault (Figure 16), which is not a consistent pattern of fault displacement. For those two reasons it was very plausible that there was a problem in the interpretation of the fault 4. So it was necessary to check the interpretation of fault 4 again. The re-interpretation of fault 4 will be shown in the discussion chapter.

In Figures 18e-o, the plots for faults with strike NW-SE (middle) show lower strain values than those for faults with strike NE-SW (right). The only exceptions are coal seams 115 and 155 (Figures 18g and 18o). The right side plots show the faults that belong mainly to the DFTAB domain, while the middle plots show the faults that belong to the other 3 fault domains.

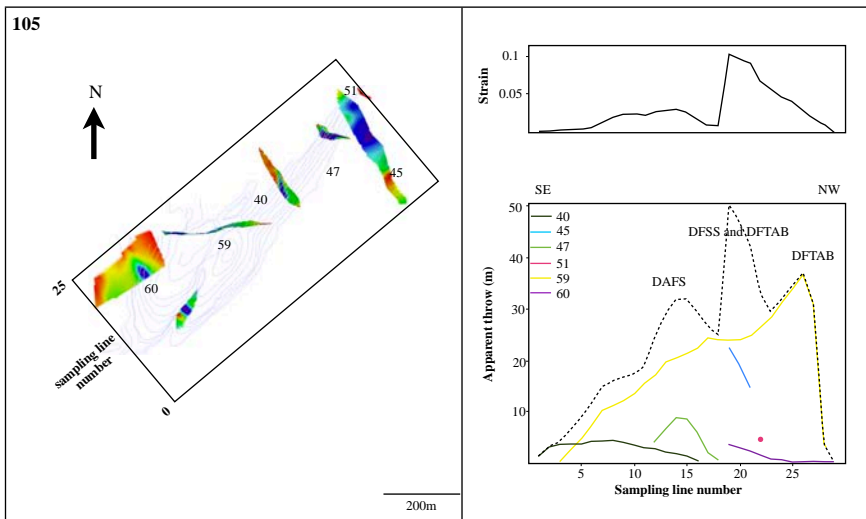




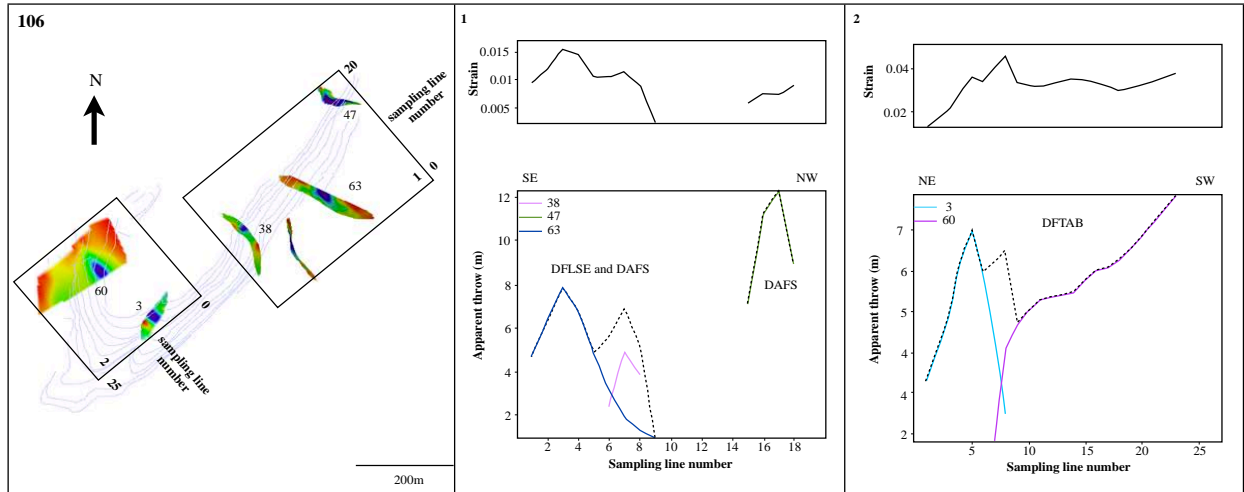
b



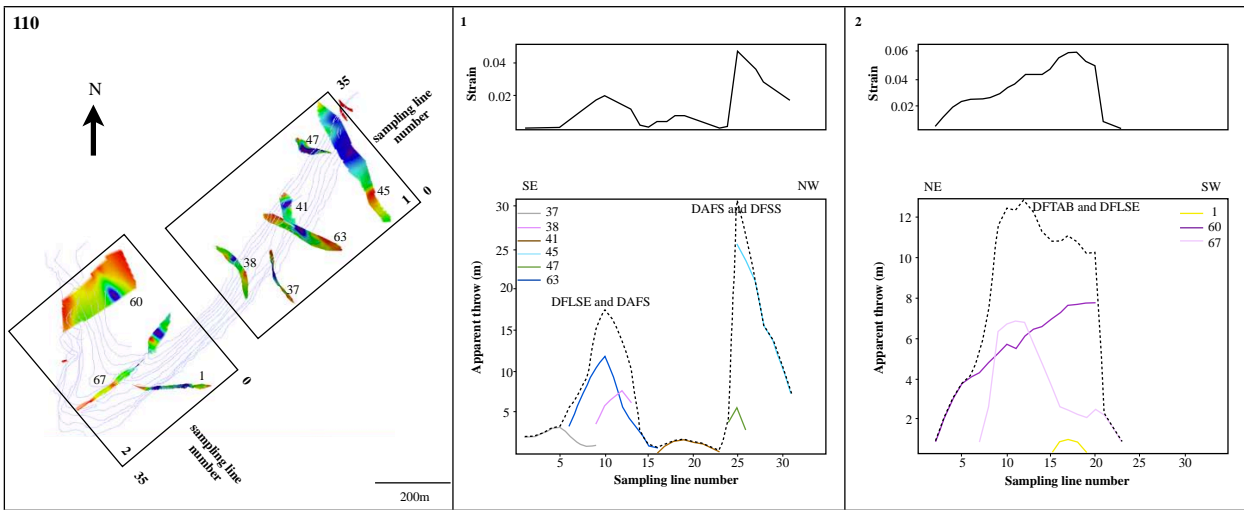
c



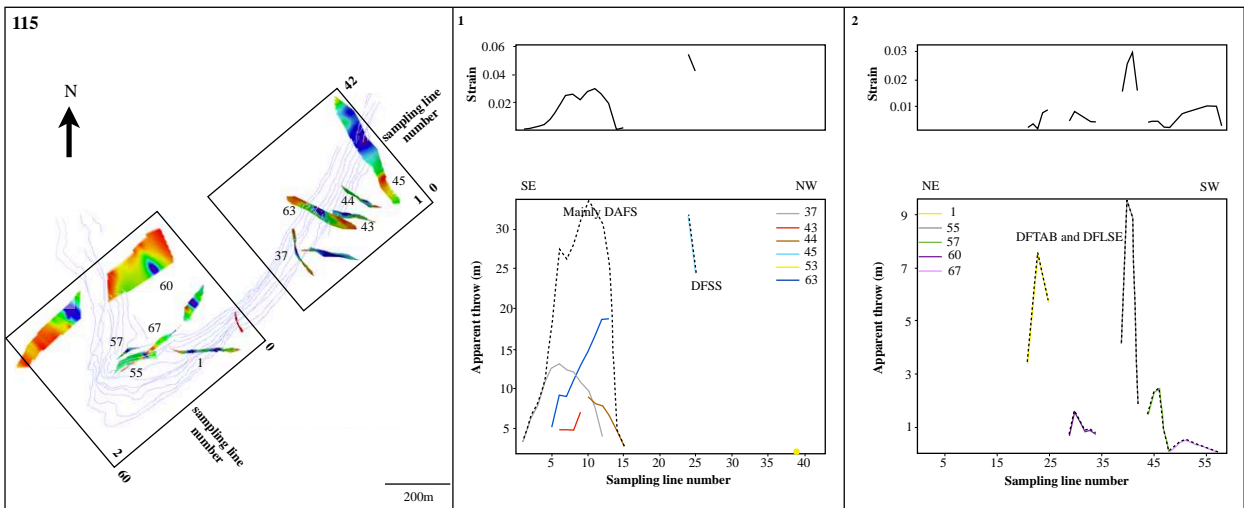
d



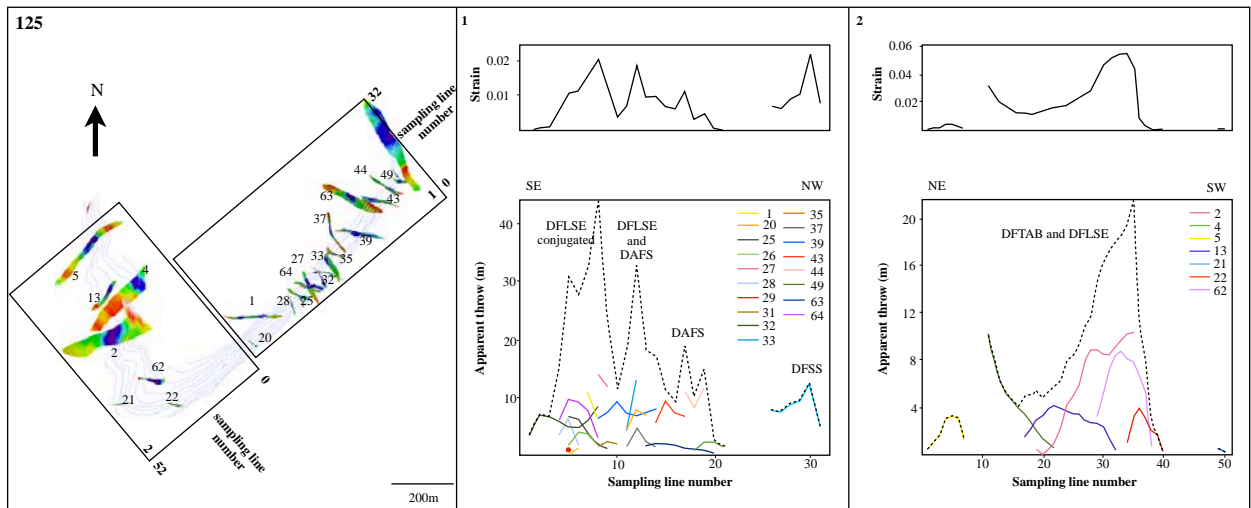
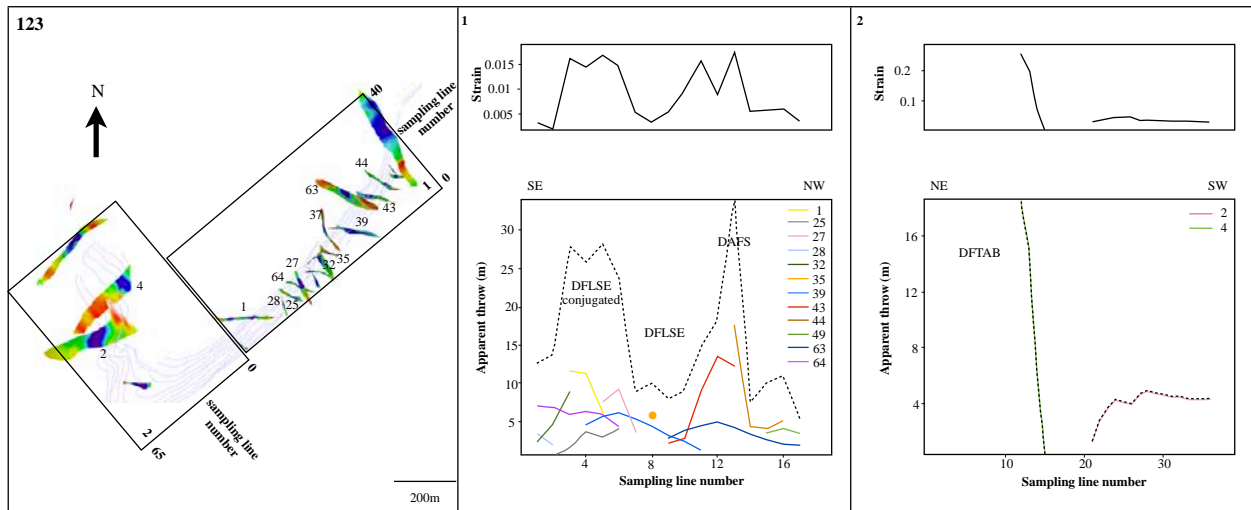
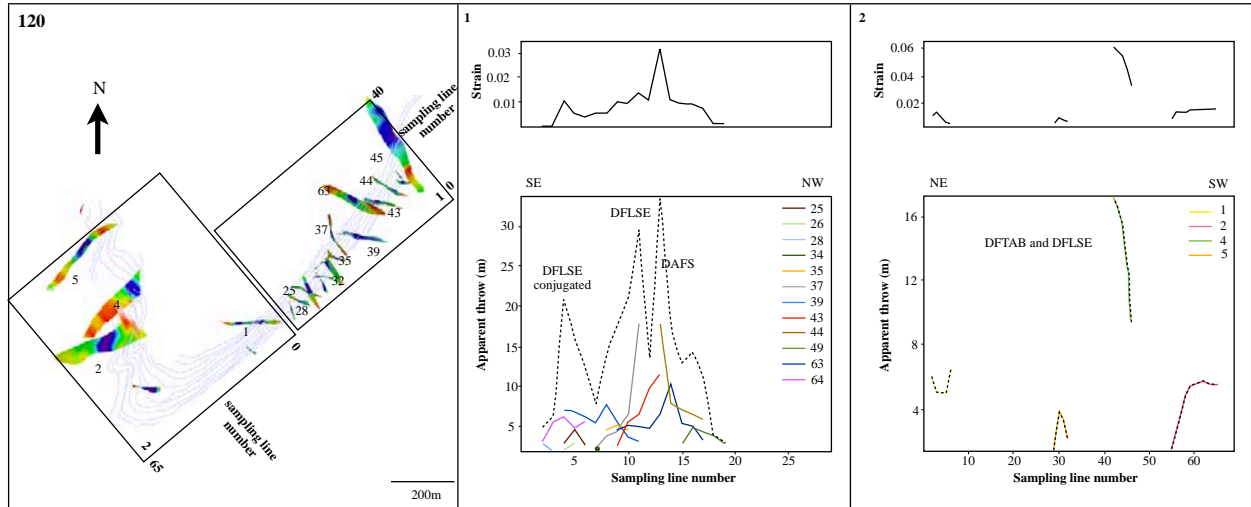
e



f



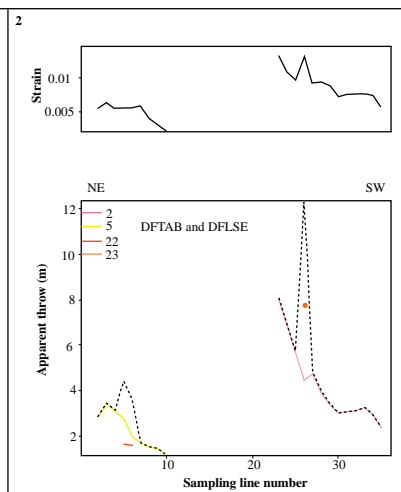
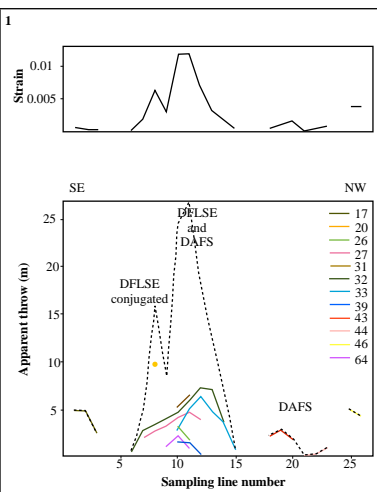
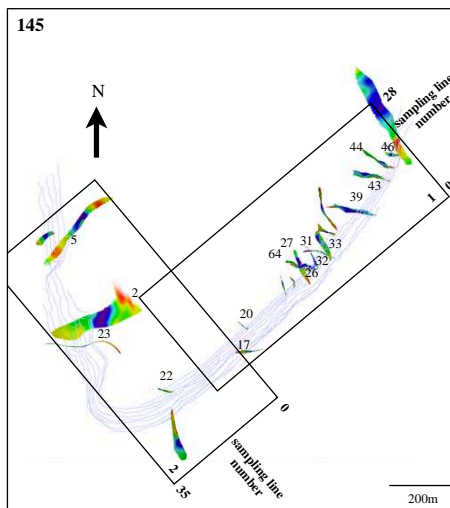
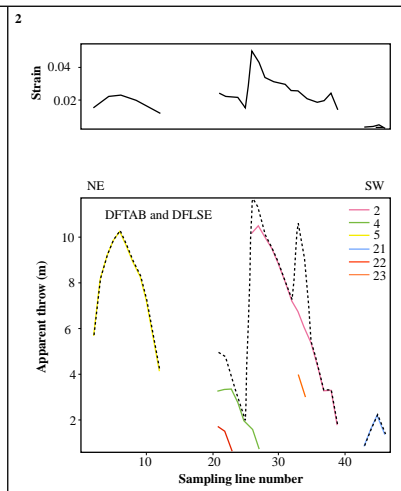
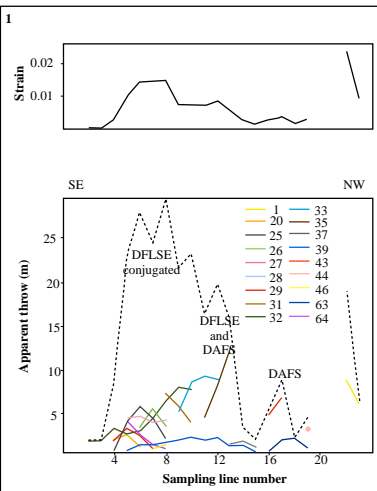
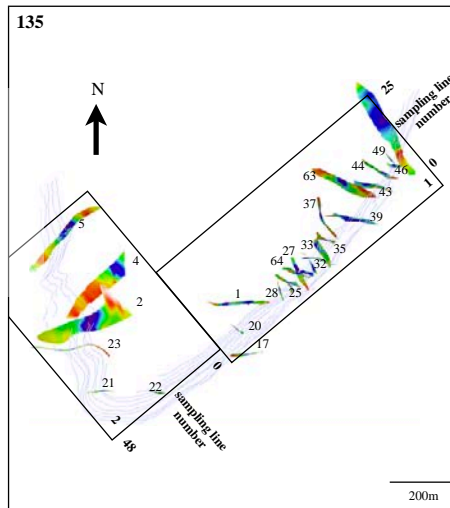
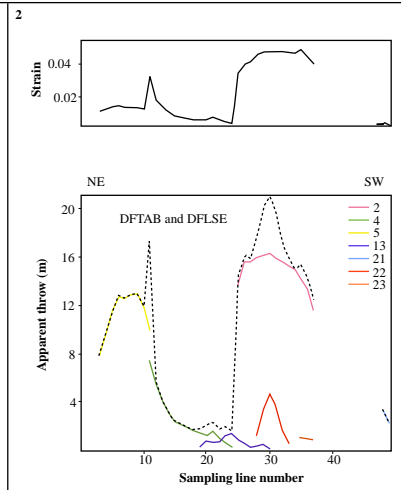
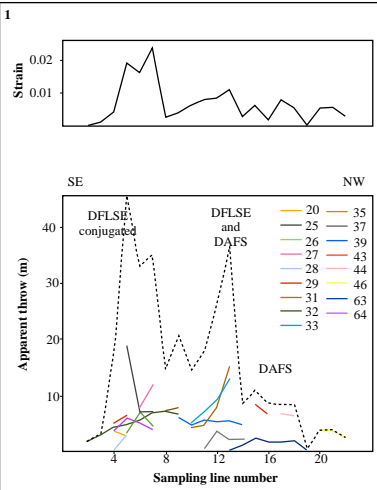
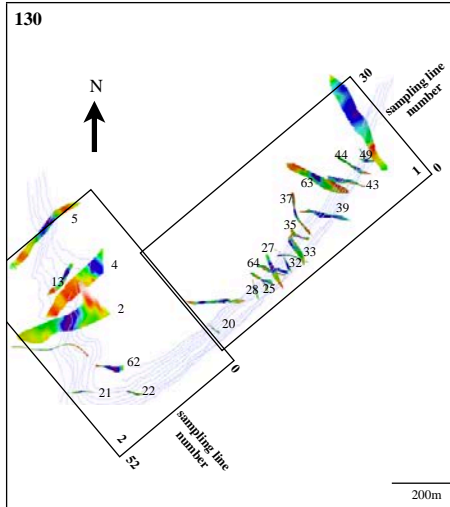
g



h

i

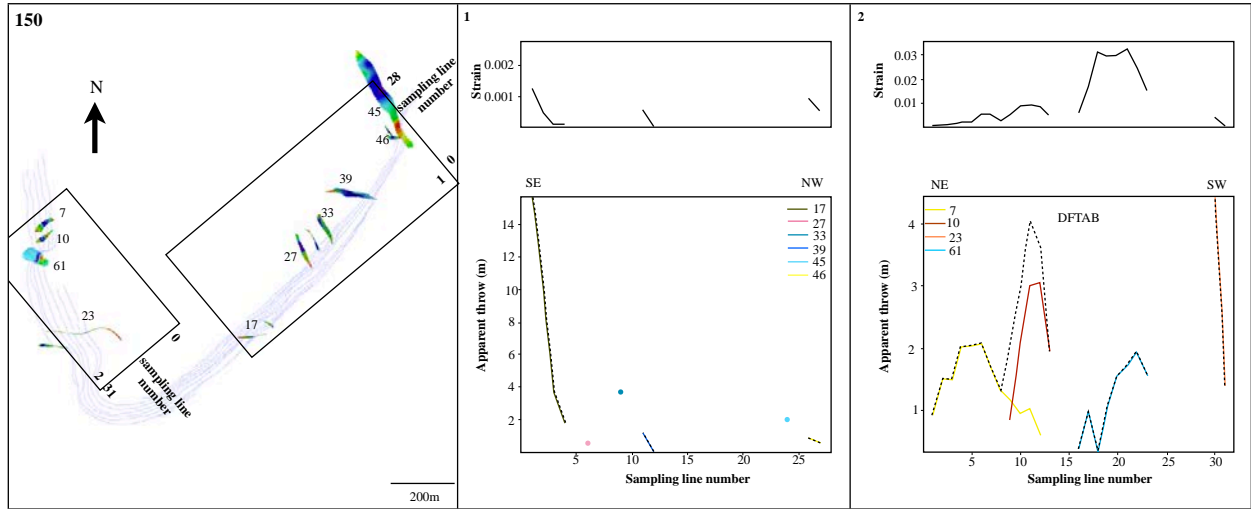
j



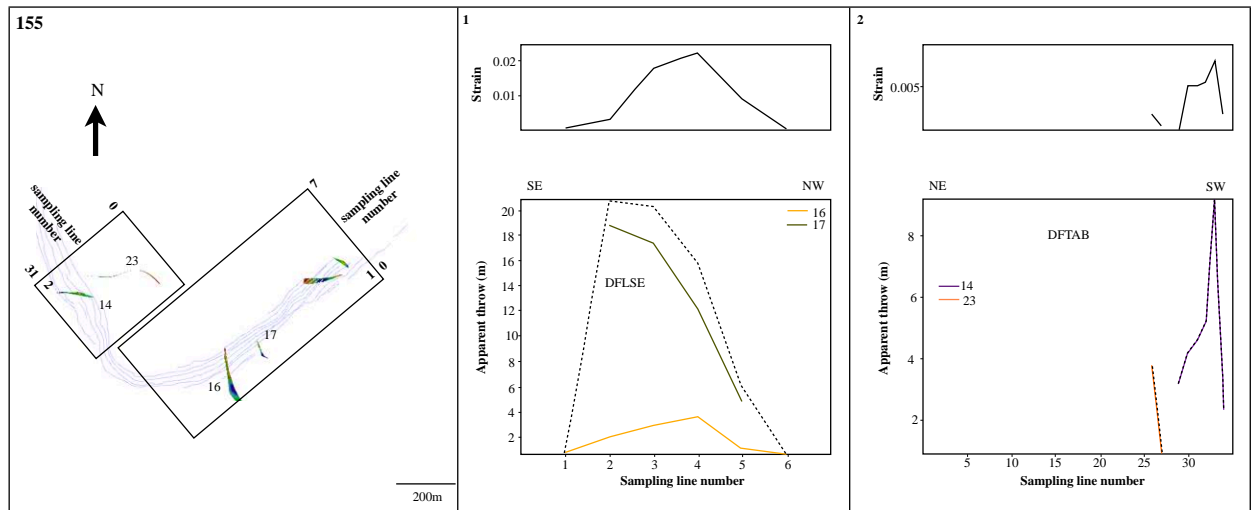
k

l

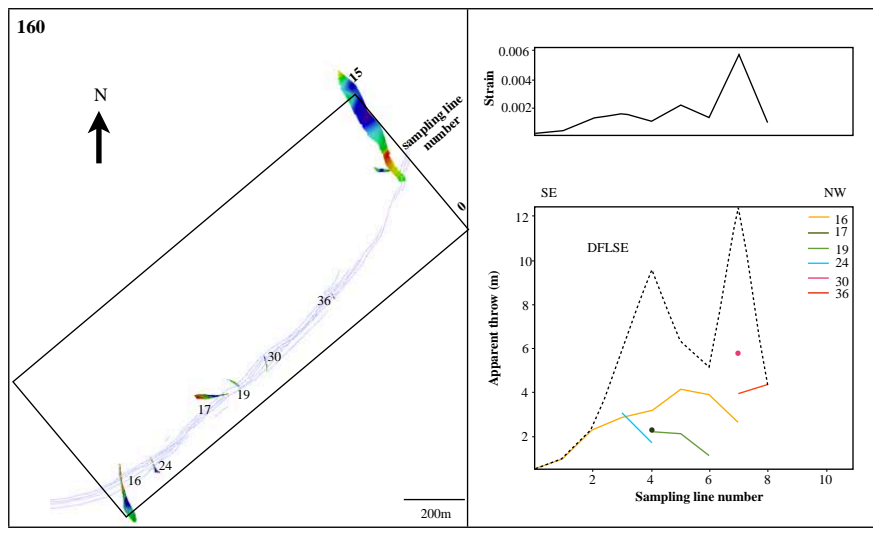
m



n



o



p

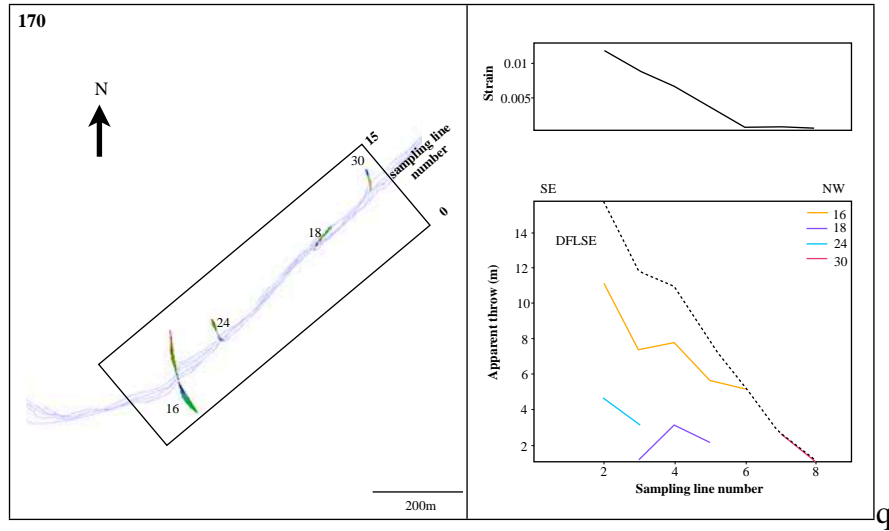


Figure 18. Left side contains maps displaying the faults affecting each coal seam contoured by their throw attribute. Right side shows plots of individual and aggregate fault throw, and fault related strain vs. distance. The initial and the last position of the sampling line are indicated in the map view. **e-o** contain two groups of plots, 1 and 2, corresponding to NW-SE striking faults (1) and NE-SW striking faults (2). DFTAB : Tabaco fault domain, DFLSE: Southern limb domain, DAFS: Samán fault antithetic domain, DFSS: Samán fault domain.

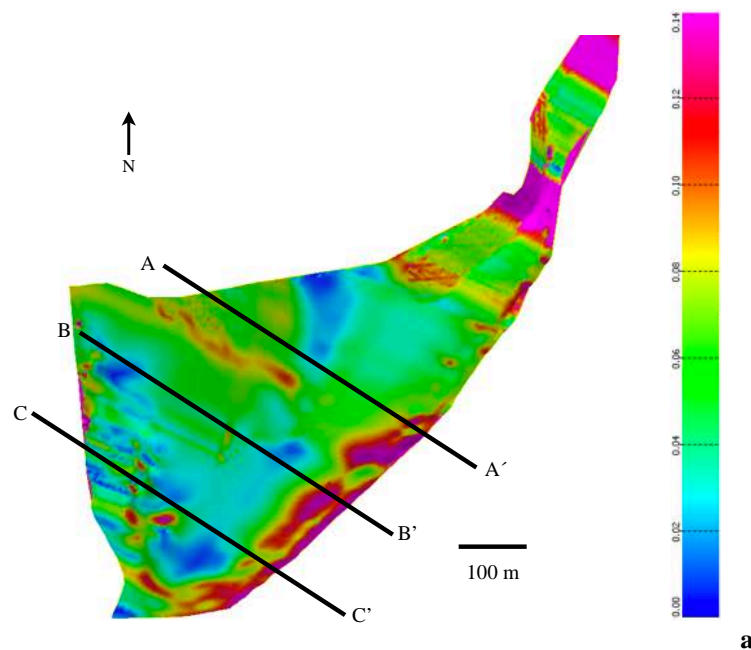
4.3 Restoration

Figure 19 shows the results of the restoration of the anticline using the flexural-slip technique. At each restoration stage, the uppermost stratigraphic surface was unfolded to a datum (300 m) while the underlying surfaces were carried as passive objects. The underlying layers were sequentially unfolded as the restoration proceeded. Since the older beds have more control data, the restoration was performed only in this part. The coal seams that were included in the restoration are 130, 115, 105 and 100. Figure 19 shows the incremental restoration of 3 cross sections through the anticline. When the restoration was done, the strain was captured in the restored beds (Figure 19a). Strain maps from the unfolding will be explained in the next section.

The coal seams were restored incrementally through four unfolding stages. The total shortening of the anticline is 18%. The shortening of the restoration of coal seam 130 is 6%, of coal seam

115 is 2%, of coal seam 105 is 7%, and of coal seam 100 is 3% (Figure 19). Shortening was measured across the surface in the maximum shortening direction (127°) normal to the fold axis.

When coal seam 130 was restored, the main fold disappears almost completely. This suggests that the fold was formed after the deposition of the the Cerrejón Formation. However after the restoration of coal seam 130, it is still possible to observe some minor folds in coal seams 105 and 100 (Figure 19b left side). The restoration shows that: 1) flexural slip was not the only deformation mechanism that operated in the anticline. Flexural slip is an important mechanism in systems consisting of mechanically strong layers and beds of easy slip such as thinly bedded sandstone-shale sequences (Lisle, 1999). In the older coal seams (95-105) this interbedding between strong layers and incompetent beds is not observed (Figure 4), and for that reason the slip between those older beds may not easily happen. 2) Small scale folding occurs in coal seams 100 and 105 located in a sedimentary package surrounded by shale, and claystone (Figure 4). This material is very ductile and can flow relatively easy. Despite minor folds in coal seams 100, 105 and 115, after the restoration of coal seam 130, the regional dip is towards the west (Figure 19b right side). The same regional dip is observed after the restoration of coal seams 115 and 105 (Figure 19b left side).



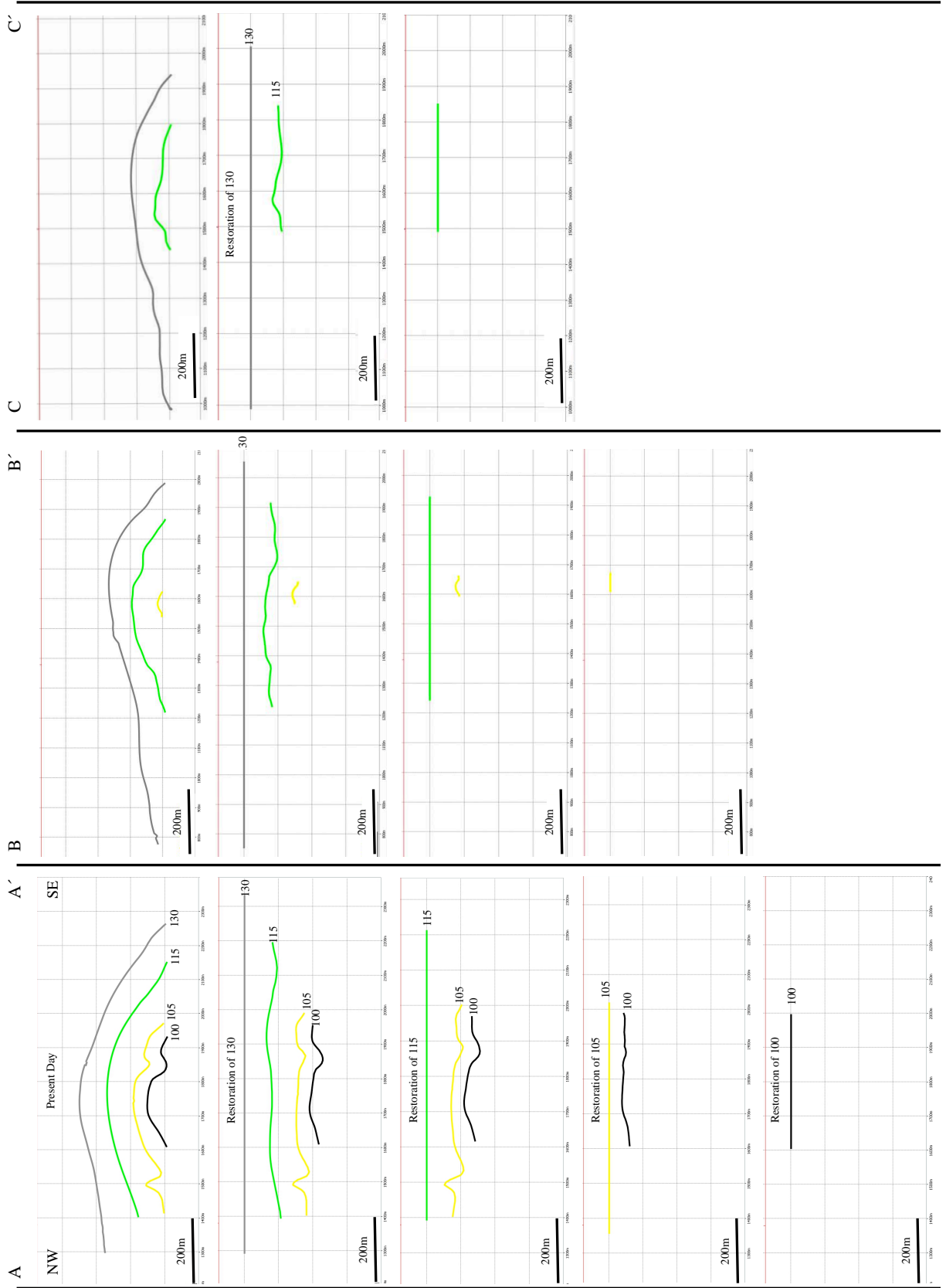


Figure 19. Restoration of the Tabaco anticline using the flexural-slip technique. The cross-

b

sections have no vertical exaggeration. a) plan view of the horizon 130 with the position of the cross sections. The colors indicate maximum principal elongation e_1 (which is explain in the next chapter) b) Left side: Restoration stages in cross section A-A' showing the present-day geometry, the restoration of coal seam 130, restoration of coal seam 115, restoration of coal seam 105 and restoration of coal seam 100. Note that in the present day section some small change of stratigraphic thickness across the fold can be observed. In the middle of the figure: Restoration stages in cross section B-B' showing the present-day geometry, restoration of coal seam 130, restoration of coal seam 115 and restoration of coal seam 105. Right side: Restoration stages in cross section C-C' showing the present-day geometry, the restoration of coal seam 130 and restoration of coal seam 115.

4.3.1 Strain maps

When the restoration was done the strain was captured in the model beds between restoration steps. The principal strain orientations were calculated using Move (Midland Valley). It is calculated using the coordinate position from the strained coal seams relative to the position of unstrained coal seams. The xyz position is given for each principal strain axes e_1 , e_2 and e_3 . Figure 20 shows the values of maximum principal elongation e_1 for coal seams 130, 115, 105 and 100, which was captured between restoration steps. After the restoration of coal seam 130 the main fold disappears almost completely (Figure 19b), and for that reason the strain captured in coal seams 130 and 115 (Figures 20a and b) is mainly associated with the bigger scale of folding, while the strain captured in coal seams 105 and 100 (Figures 20c-d) is mainly associated with small scale folding. A common characteristic in coal seams 130 and 115 is an area of high strain values located in the SE limb (Figures 20a and b), which has the steeply dipping strata. The shallow, W-dipping limb shows relative lower values of strain in coal seams 130 and 115 (Figures 20a and b). Additionally coal seams 130 and 115 show a localized area of high strain in the SW limb, where faults striking NE-SW are located (arrows in Figures 20a-b).

Coal seams 100 and 105 show an area of high strain with orientation approximately E-W (arrows in Figures 20c and d). Those areas of high strain in coal seams 100 and 105 may correspond with the minor folds, which remain after the restoration of coal seam 130 (Figure 19b). Coal seam 105 shows higher values of e_1 than the other coal seams. When the restoration was done, it was also the coal seam with the highest values of shortening (7%). The cross-section A-A' in figure 19b

shows that coal seam 105 is the one with more amount of minor folds, indicating a higher shortening compared with the others coal seams.

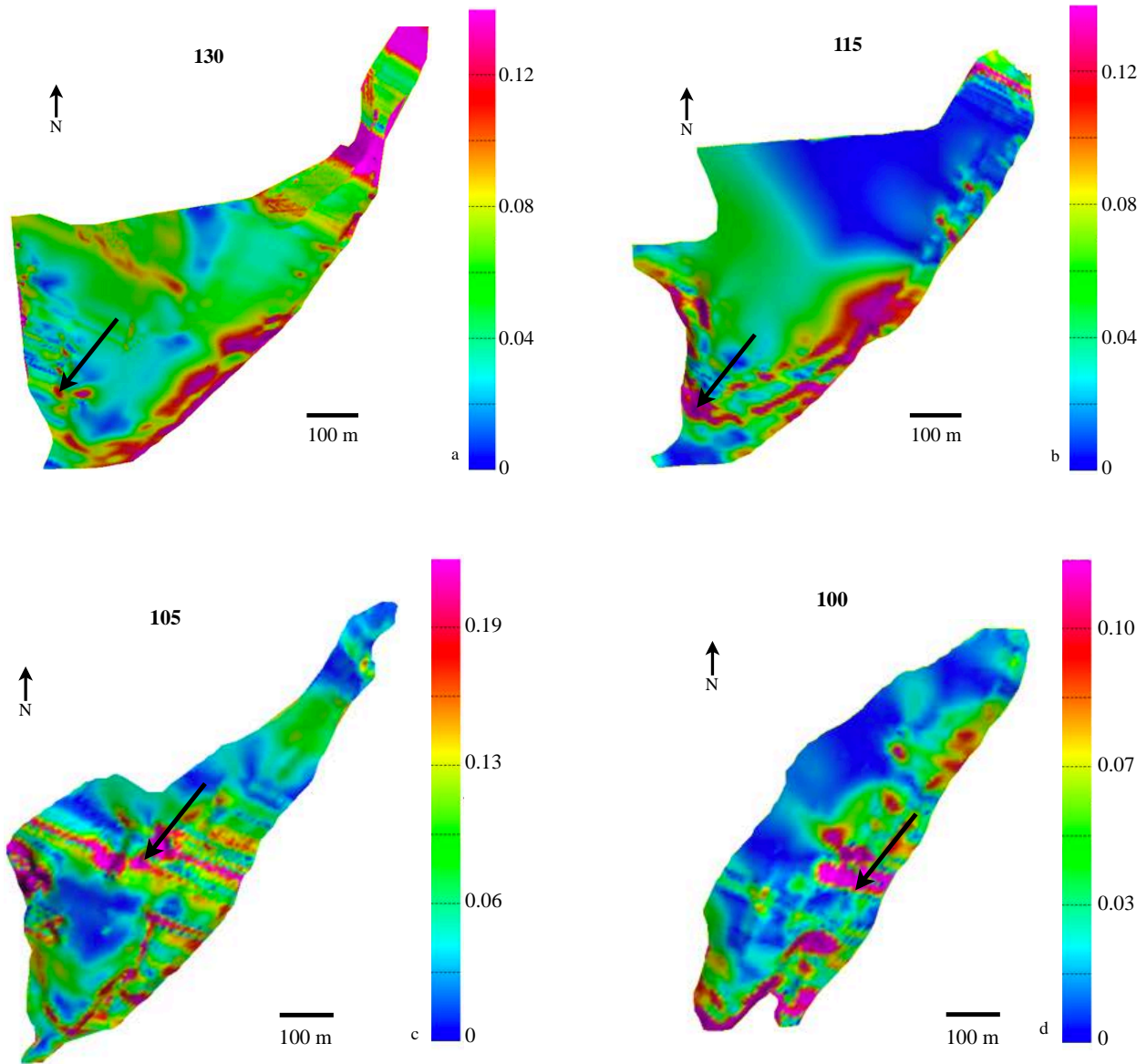


Figure 20. Maps of maximum principal elongation e_1 . a) coal seam 130 b) coal seam 115 c) coal seam 105 and d) coal seam 100. The strain was captured between restoration steps.

5. Discussion

The 3D model shows a total of 67 faults distributed in 17 coal seams. The amount of faults affecting the older coal seams are lower (in coal seams 95, 100, 102, and 105 the number of faults are 4, 7, 6, and 7 respectively) than in intermedium coal seams (in coal seams 125 and 130 there are 29 faults). After coal seam 130, the number of faults decrease. The lower amount of faults in the lower coal seams can be the result of the incompetence of the rocks surrounding these coal seams (Figure 4). Furthermore, it seems like the faults are splitting upsection in the anticline, with the lower beds having few fault branches while the intermedium beds have more fault branches (Figures 14 and 18). Since the lithology of the upper coal seams is almost the same as that of the intermedium coal seams, the number of faults in these coal seams (e.g. 160 and 170) can be the same as in the intermedium seams. However, because there are less data in the upper beds, it is not possible to test this hypothesis.

In the 3D model, it was also possible to observe a series of reverse faults with an E-W direction at the south nose of the plunging anticline, between coal seams 115 and 145 (Figure 14). A possible origin for these faults is a N-S compressional event proposed by Kellogg (1984) in the Sierra de Perijá. This event, which is post-middle Eocene, generated stylolites, folds and reverse faults with an E-W direction. Kellogg (1984) suggested that this event may be caused by oblique movement on the Oca fault system.

A conjugated pattern was described in the eastern limb of the anticline, between coal seams 120 to 145. Conjugated fractures are common in folded strata (Stearns, 1968; Cooper et al., 2006). These conjugates are formed systematically with respect to the fold axis and bedding (Stearns, 1968; Bergbauer and Pollard, 2004) (Figure 21). The conjugated faults described in the Tabaco anticline may have been generated when the strata of the anticline were folded.

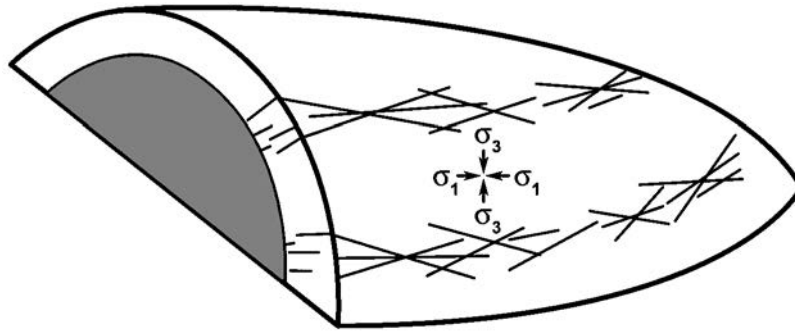


Figure 21 Stearn and Friedman (1972) model, showing the fractures set associated with folding (Cooper et al., 2006).

Four different fault patterns in the contours of fault throw were observed (Figures 16 and 17): 1) Low throw in the middle of the fault and high throw in the areas around, 2) highest throw at one corner of the fault and not in the center, 3) the most common pattern, highest throw in the middle of the fault, and 4) in conjugated faults the highest value of throw is located at the intersection of the two fault planes. Those throw patterns were not only a useful technique for checking the quality of the interpretation and construction of the 3D model, but they also help to understand fault growth patterns and the interaction between faults.

The fault plane with an area of low throw in the middle of the fault can indicate: 1) that the area of low throw is a tip point, which suggest two instead of one fault, 2) the linkage fault model (Peacock and Sanderson, 1991; Cartwright et al., 1995; Kim et al., 2000), in which the faults grew isolated at early stages and then linked to produce a larger fault, and 3) areas of high displacement due to the intersection of two faults with different orientation (Kim and Sanderson, 2005). After a careful review of the interpretation, options 1 and 3 were discarded, so for the Tabaco anticline, the most likely alternative is the linkage fault model.

The second pattern is a fault plane with the area of highest throw value in a corner of the fault and not in the center. This suggests: 1) that the fault plane is not complete because there were not enough data to cover it. 2) In the case of fault 4, there is a problem in the interpretation because it is not a consistent pattern of fault displacement. Additionally, the fault-related strain value for this fault was 0.2, higher than the upper limit of 0.1 suggested by Freeman et al. (2010). When

the faults-horizons intersections polygons were re-checked in the 3D model an anomalous high value in the displacement of this fault was observed, so a re-interpretation of fault 4 was done. The new values of throw and fault-related strain for fault 4 in coal seam 123 can be seen in figure 22. The highest value of fault-related strain is 0.09 in this case, which is consistent with the upper limit suggested by Freeman et al. (2010). With this result it is clear that the fault throw pattern and fault-related strain values were a very useful tool to validity the fault interpretation.

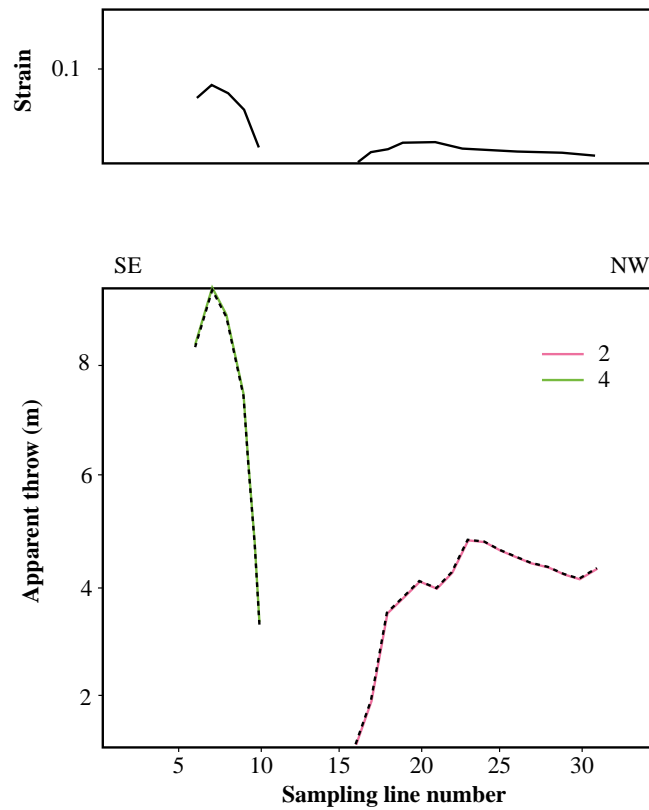


Figure 22 Individual and aggregate fault throw, and fault-related strain vs. distance for coal seam 123 after the re-interpretation of fault 4.

The third pattern with high throw values in the middle of the fault shows a gradual variation in throw along strike, which is the expected behavior of a single fault. The last pattern occurs in conjugated faults. In these cases, the highest value of throw is located at the intersection of the two fault planes.

The fault domain that have the highest values of strain is the DFTAB, showing strain values (fault-related strain) between 0.5% for coal seam 155, to 9% in coal seam 123 (Figure 18i and 18o). The strike of the faults in this domain is mainly NE-SW, similar to the trend of the Perijá mountains. This can indicate a propagation of the Perijá deformation towards the west. However there is one fault in the DFTAB domain that does not have the NE-SW trend. Fault 59 in the northern part of the DFTAB domain and in lower coal seams, strikes almost E-W (Figure 14, coal seam 100-105). Two interpretations are possible for the strike of this fault. The first interpretation is that this fault was generated in the N-S compressional event described above. The other option is that this part of the anticline is affected by left lateral movement of the Samán fault, which rotated fault 59 to its current position. This second interpretation is supported by the shape of the axis of the anticline, which bends close to the area of the Samán fault (Figure 2).

For coal seam 130 the curvature values are showing a difference between the size of the basins (dark red) and synformal saddles (dark yellow), in both limbs. In the western limb the basins are bigger than those in the eastern limb (Figure 15). The eastern limb has more faults affecting this area of the coal seam (Figure 14), so this situation does not allow the development of big basins in the eastern limb. While the faults affecting the western limb are less but with a higher displacement, making that the size of the basins and synformal saddles bigger in that part of the anticline.

The Cerrejón formation is a pre-folding formation, because when the upper coal seam 130 was restored, the anticline almost vanished. The total shortening of the Tabaco anticline calculated with the flexural slip technique is 18%. The shortening in the restoration of coal seam 130 is 6%, of coal seam 115 is 2%, of coal seam 105 is 7%, and of coal seam 100 is 3%. In the restoration process, a regional dip towards the west was identified. This shows that the depocenter of the basin at the onset of folding was to the west of the Tabaco anticline .

When the shortening calculated with flexural slip is compared with the fault-related strain, it does not show significant difference (in most cases only 1%). The maximum fault-related strain for coal seam 130 is 5% (Figure 18 k), for coal seam 115 is 3% (Figure 18 g), for coal seam 105 is 10 % (Figure 18 d), and for coal seam 100 is 2.5% (Figure 158b). Fault-related strain, can be slightly different that the fold-related strain calculated with flexural slip, because the gradual accumulation of regional strain leads to fault slip; therefore the fault-related strain is related to local perturbations superimposed on the regional strain (Dee et al., 2007).

High strain values (ϵ_1 , Figure 20a and b) are located in the SE limb associated with the steeply dipping strata in coal seams 130 and 115. Coal seams 100 and 105 show an area of high strain with orientation E-W (arrows in Figure 20c and d). The strain captured in coal seams 130 is mainly associated with the bigger scale of folding, while the strain captured in coal seams 105 and 100 (Figures 20c-d) is mainly associated with small scale folding. The high values of strain in coal seams 130 and 115 shows that the SE limb with steeply dipping strata accommodated the highest amount of strain in the anticline.

5. 1 Summary of the main events affecting the Tabaco anticline in a regional context

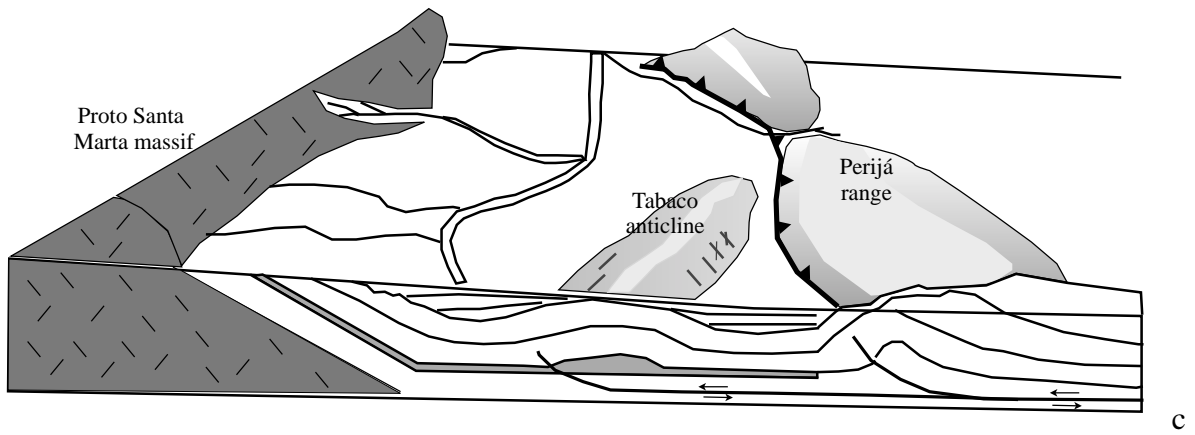
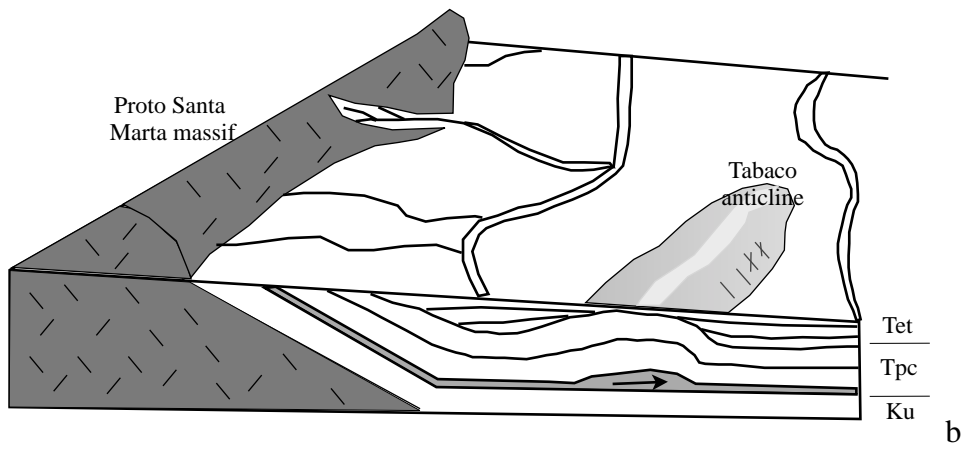
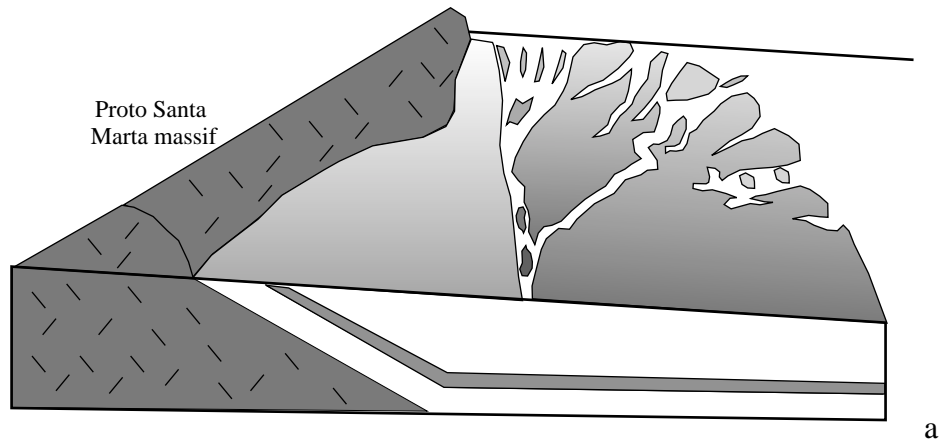
In the Middle-to-Late Paleocene the deposition of the Cerrejón Formation started in the area (Figure 23a). The depocenter was towards the west of the future position of the Tabaco anticline. Even though some small thickness changes are identified in the Cerrejón Formation, it is a pre-folding unit. By that time, the Santa Marta massif had some episodes of uplift (Cardona et al., 2010).

In the Late Paleocene-Early Eocene, the deposition of the Tabaco Formation started in the basin. Montes et al. (2010) interpreted this Formation as syntectonic. If so, the Tabaco anticline was probably formed during this time. The Santa Marta massif continued its uplift (Cardona et al., 2010). Bayona et al. (2007) and Kellogg (1984) suggested that the tectonic activity of the Perijá

range started in the Early-Middle Eocene. The vergence of the faults in the western part of the Perijá range is towards the west, however the vergence of the Tabaco anticline is towards the east. One possible explanation can be that the Tabaco anticline was formed by a backthrust of the west vergent thrust belt of the Perijá range (but there is not evidence of this backthrust). However in the western limb of the Tabaco anticline, a series of thrust (belonging to the DFTAB domain) with the same strike and the same vergence as the Perijá thrust belt are observed. So an alternative interpretation for the formation of the anticline is that it was generated as a detachment fold, triggered by the uplift of the Santa Marta massif and using the incompetent Cerrejón formation as a detachment (Figure 23b). In addition, the reverse faults in the western limb of the anticline could be generated after the anticline was formed and were related with the propagation of the Perijá mountain front towards the west. This second alternative can explain the eastern vergence of the anticline and the reverse faults in its western limb (Figure 23c). However with the information analyzed in this thesis, there is not evidence that the faults of the western limb are posterior to the main fold event.

The conjugated faults were generated when the beds of the Cerrejón Formation were folded (Figure 23b). This conjugated pattern include two orientation of thrust faults and can be reflecting locally developed of bending or buckling (Stearns, 1968 and Bergbauer and Pollard, 2004), so it is related with the folding of the beds.

The Samán fault may be formed in an event posterior to the formation of the Tabaco anticline and the generation of the faults of the DFTAB domain. This left lateral strike-slip fault generated a series of small antithetic faults close to its area of influence. Additionally, it bent the axis of the anticline and some the faults of the DFTAB domain (Figures 2 and 23d). Another event posterior to the formation of the Tabaco anticline was the generation of the E-W faults generated by a north-south compression event (Figure 23d).



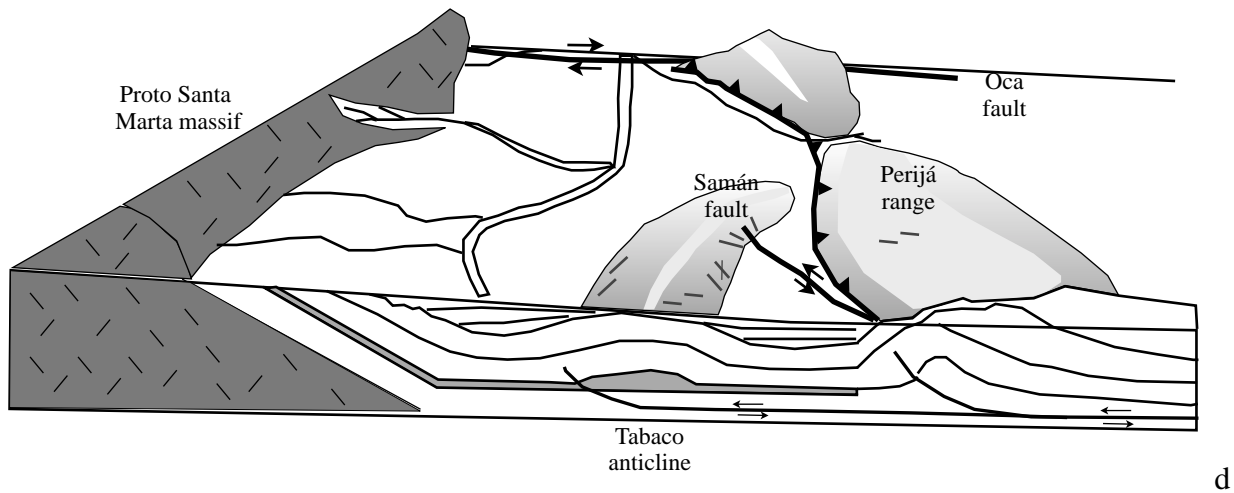


Figure 23 Summary of the main events affecting the Tabaco anticline. a) Middle-to-Late Paleocene deposition of the Cerrejón Formation. b) Late Paleocene-Early Eocene generation of the Tabaco anticline as a detachment fold, Ku: Cretaceous undiff., Tpc: Cerrejón Formation, Tet: Tabaco Formation. c) Reverse faults in the western limb of the anticline are generated and are related with the propagation of the Perijá mountain front towards the west. Perijá range is interpreted here as thin-skin due to the structural cross section from Montes et al. (2010) and Kellogg (1984) d) The Samán strike-slip fault generated antithetic faults in the anticline and bends it. Faults striking E-W are also generated.

References

Allmendinger, R.W., Cardozo, N., Fisher, D., 2012. Structural Geology Algorithms. Cambridge University press. 289 p.

Bayona, G., Lamus, F., Cardona, A., Jaramillo, C., Montes, C., and Tchegliakova, N., 2007. Procesos orogénicos del Paleoceno para la Cuenca de Ranchería (Guajira, Colombia) definidos por análisis de procedencia. Geol. Colomb., 32, p 21-46.

Bayona, G., Montes, C., Cardona, A., Jaramillo, C., Ojeda, G., Valencia, V., Ayala-Calvo, C., 2011. Intraplate subsidence and basin filling adjacent to an oceanic arc-continent collision: a case from the southern Caribbean-South America plate margin. Basin research, 23, p 403-422.

Beck, E., 1921. Geology and Oil Resources of Colombia, South America, *Economic Geology*, 16, p 463-465.

Bergbauer, S., 2002. The use of curvature for the analysis of folding and fracturing with application to the Emigrant Gap Anticline, Wyoming. PhD thesis, Stanford University.

Bergbauer, S., and Pollard, 2004. A new conceptual fold-fracture model including pre-folding joints, based on the Emigrant Gap anticline, Wyoming. *GSA Bulletin*, 116, p 294-307

Cardona, A., U. Cordani., and McDonald, W., 2006. Tectonic correlations of pre-Mesozoic crust from the northern termination of the Colombian Andes, Caribbean region. *Journal of South American Earth Sciences*, 21, p 337–354.

Cardona, A. Valencia, V., Reiners, P., Duque, J., Montes, C., Nicolescu, S., Ojeda, G., Ruiz, J., 2008. Cenozoic Exhumation of the Sierra Nevada De Santa Marta, Colombia: Implications on the Interactions Between the Caribbean and South American Plate. 2008 Joint Meeting of The Geological Society of America, Soil Science Society of America, American Society of Agronomy, Crop Science Society of America, Gulf Coast Association of Geological Societies with the Gulf Coast Section of SEPM.

Cardona, A., Valencia, V., Bayona, G., Duque, J., Ducea, M., Gehrels, G., Jaramillo, C., Montes, C., Ojeda, G., Ruiz, J., 2010. Early-subduction-related orogeny in the northern Andes: Turonian to Eocene magmatic and provenance record in the Santa Marta Massif and Rancheria Basin, northern Colombia. *Terra Nova*, 0, p 1-9.

Cardozo, N. and Allmendinger, R.W., 2013. Spherical projections with OSXStereonet. *Computers and Geosciences*, 51, p 193-205.

Cartwright, J.A., Trudgill, B.D., Mansfield, C.S., 1995. Fault growth by segment linkage: an explanation for scatter in maximum displacement and trace length data from the Canyon-lands Grabens of SE Utah. *Journal of Structural Geology*, 17, p 1319 – 1326.

Cooper, S., Goodwin, L., Lorenz, C., 2006. Fracture and fault patterns associated with basement-cored anticlines: The example of Teapot Dome, Wyoming. *AAPG Bulletin*, 90, p 1903-1920.

Dee, S. J., Yielding, G., Freeman, B., Healy, D., Kuszniir, N., Grant, N., and Ellis, P., 2007. Elastic dislocation modelling for prediction of small-scale fault and fracture network characteristics. In Lonergan L. et al. (Eds). *Fractured reservoirs*. Geological Society, Special Publication, 270, p 139-155.

Duerto, L., Escalona, A., Mann, P., 2006. Deep Structure of the Mérida Andes and Sierra de Perijá Mountain Fronts. *AAPG Bulletin*, 90, Maracaibo basin, Venezuela, p 505–528.

D'Errico, J., 2005. Surface Fitting using gridfit (<http://www.mathworks.com/matlabcentral/fileexchange/8998>), MATLAB Central File Exchange. Retrieved May 18, 2006.

Feo-Codecido, G., 1972. Contribución a la estratigrafía de la Cuenca Barinas-Apure. *Mem. IV Congr. Geol. Venez., MMH, Direc. Geol., Publ. Esp. N° 5, 11*, p 773-782.

Fernandez, O., 2005. Obtaining a best fitting plane through 3D georeferenced data. *Journal of Structural Geology*, 27, p 855-858.

Fisher, Q.J. and Jolley, S.J., 2007. Treatment of faults in production simulation models. In Jolley, S.J., Barr, D., Walsh, J.J. and Knipe, R.J. (Eds). *Structurally Complex Reservoirs*. Geological Society of London, Special Publication 292, p 219-233.

Fossen, H., 2012. *Structural Geology*. Cambridge University Press. 463 p.

Freeman, B., Boulton P., Yielding G., Menpes, S., 2010. Using empirical geological rules to reduce structural uncertainty in seismic interpretation of faults. *Journal of Structural Geology*, 32, p 1668-1676.

Griffiths, P., Jones, S., Salter, N., Schaefer, F., Osfield, R., Reiser, H., 2002. A new technique for 3D flexural-slip restoration. *Journal of Structural Geology*, 24, p 773-782.

Huggins, P., Watterson, J., Walsh, J. J. & Childs, C., 1995. Relay zone geometry and displacement transfer between normal faults recorded in coal-mine plans. *Journal of Structural Geology*, 17, p 1741-1755.

Jaramillo, C., Pardo, A., Rueda, M., Harrington, G., Bayona, G., Torres, V., Mora, G., 2007. Palynology of the Upper Paleocene Cerrejon formation, Northern Colombia. *Palynology*, 31, p 153-189.

Kellogg, J. N., 1984. Cenozoic tectonic history of the Sierra de Perijá, Venezuela-Colombia, and adjacent basins. In W. E. Bonini, Hargraves, R. B. and Shagam, R., ed., *The Caribbean-South American plate boundary and regional tectonics*, v. Memoir 162, Geological Society of America, p 239-261.

Kellogg, J.N., Bonini, W.E., 1982. Subduction of the Caribbean plate and basement uplifts in the overriding South American plate. *Tectonics*, 1, p 251–276.

Kim, Y-S., Sanderson, D., 2005. The relationship between displacement and length of faults: a review. *Earth-Science Reviews*, 68, p 317-334.

Lisle, R., 1999. Predicting patterns of strain from three-dimensional folds geometries: neutral surface folds and forced folds. In Ameen, M., Cosgrove, J., eds., *Forced Folds And Fractures: The Geological Society Special Publication*, 169, p 213-222

MacDonald, W., Doolan, B. and Cordani, U., 1971. Cretaceous-Early Tertiary metamorphic age values from the South Caribbean. *Geol. Soc. Am. Bull.*, 82, p 1381–1388.

Montes, C., Guzman, G., Bayona, G., Cardona, A., Valencia, V., Jaramillo, C., 2010. Clockwise rotation of the Santa Marta massif and simultaneous Paleogene to Neogene deformation of the Plato-San Jorge and Cesar-Ranchería basins. *Journal of South American Earth Sciences*, 29, p 832-848.

Montes, C., Palencia, J., Ruiz, M.C., Zapata, S., in prep. Dissection of the Tabaco anticline: Detailed record using DGPS.

Mynatt, I., Bergbauer, S., Pollard, D., 2007. Using differential geometry to describe 3-D folds. *Journal of Structural Geology*, 29, p 1256-1266.

Palencia, A., 2007. Análisis estructural y geométrico del anticlinal de Tabaco en la mina del Cerrejón, Guajira. Undergraduate Thesis, Universidad EAFIT, 108 pp.

Peacock, D.C.P., Sanderson, D.J., 1991. Displacement and segment linkage and relay ramps in normal fault zones. *Journal of Structural Geology*, 13, p 721–733.

Pindell, J. L., Higgs, R., and Dewey, J. F., 1998. Cenozoic palinspastic reconstruction, paleogeographic evolution and hydrocarbon setting of the northern margin of South America. In Pindell, J. K., and Drake, C. L., eds., *Paleogeographic evolution and Non-glacial Eustasy, northern South America: SEPM Special Publication*, 58, p 45-8.

Pollard, D. D. & Fletcher, R. C., 2005. *Fundamentals of Structural Geology*. Cambridge University Press, 500 p.

Rippon, J.H., 1985. Contoured patterns of the throw and hade of normal faults in the Coal Measures (Westphalian) of north-east Derbyshire. *Proceedings of the Yorkshire Geological Society*, 45, p 147–161.

Ruiz, M.C., 2006. Cartografía estructural del flanco occidental del anticlinal del tajo tabaco uno en la mina de Carbones del Cerrejón. Undergraduate Thesis, Universidad Nacional de Colombia, Medellin, 78 pp.

Sánchez, C.A., 2008. Exploración geológica del pit Annex y las zonas circundantes en el piedemonte de la Serranía del Perijá. Undergraduate Thesis, Universidad Nacional de Medellin, 48 pp.

Sánchez, C.J., and Mann, P., 2012. Thick-Skinned Style and Timing of Convergent Tectonics in Northwestern South America and Implications for Petroleum Exploration. AAPG Annual Convention and Exhibition, Long Beach, California.

Shagam, R., B. Kohn, P. Banks, L. Dasch, R. Vargas, G. Rodriguez, and Pimentel, N., 1984. Tectonic implications of Cretaceous-Pliocene fission-track ages from rocks of the circum Maracaibo basin region of western Venezuela and eastern Colombia, in W. Bonini, Hargraves, R. and Shagam, R., ed., *Caribbean- South American Plate Boundary and regional tectonics*: Boulder, Colorado. Geological Society of America, p 385-412.

Stearns, D.W., 1968. Certain aspects of fractures in naturally deformed rocks, in Riecker, R.E., ed., *Rock mechanics seminar*: Bedford, Terrestrial Sciences Laboratory, p 97–118.

Stearns, D. W., and Friedman, M., 1972. Reservoirs in fractured rock, in R. E. King, ed., *Stratigraphic oil and gas fields— Classification, exploration methods, and case histories*: AAPG Memoir 16/Society of Exploration Geophysicists Special Publication, 10, p 82–106.

Trenkamp, R., Kellogg, J., Freymuller, J., Mora, H., 2002. Wide plate margin deformation, southern Central America and northwestern South America, CASA GPS observations. *Journal of South American Earth Sciences*, 15, p 157- 171.

Tschanz, C.M., Marvin, R.F., Cruz, J., 1974. Geologic evolution of the Sierra Nevada de Santa Marta area, Colombia. *Geological Society of America Bulletin*, 85, p 273–284.

Walsh, J.J., Watterson, J., 1987. Distributions of cumulative displacement and seismic slip on a single normal fault surface. *Journal of Structural Geology*, 9, p 1039–1046.

Walsh, J. J., and Watterson, J., 1988. Dips of normal faults in British Coal Measures and other sedimentary sequences. *Journal of the Geological Society, London*, 145, p 859-873.